Bioorganic Chemistry 169 (2026) 109390

Contents lists available at ScienceDirect

Bioorganic Chemistry

journal homepage: www.elsevier.com/locate/bioorg

Synthesis, antitubercular activity and computational studies of click-tethered phosphonium salts

Cedric Dzidzor Kodjo Amengor [a,*], Prince Danan Biniyam [b], Victoria Ohene-Adu [b], Kwabena Adu-Adjei [b], Michael Osei [b], Patrick Gyan [a], Paul Quansah [a], Felix Odame [c], Ernest Oyeh [d], Cyril Makafui Amengor [e], Lawrence Sheringham Borquaye [f]

[a] Department of Pharmaceutical Chemistry, Drug Discovery Unit, School of Pharmacy, University of Health and Allied Sciences, Ho, Ghana
[b] Department of Pharmaceutical Chemistry, Computational Medicinal Chemistry Unit, School of Pharmacy, University of Health and Allied Sciences, Ho, Ghana
[c] Department of Basic Sciences, School of Basic and Biomedical Sciences, University of Health and Allied Sciences, Ho, Ghana
[d] Department of Nursing, Faculty of Science, Methodist University, Ghana
[e] Department of Mathematics, College of Science, University of Ghana, Legon, Ghana
[f] Department of Chemistry, Kwame Nkrumah University of Science and Technology, Ghana

ARTICLE INFO

Keywords:
Triazoles
Phosphonium salts
Antitubercular
H37Rv
MDR-TB
Molecular dynamics
InhA inhibition

ABSTRACT

This study reports the synthesis of a library comprising three series of 21 phosphonium salt hybrids **(1a–1 g, 2a–2 g, 3a–3 g)** generated *via* a click reaction yielding 1, 2, 3-triazoles with potential antitubercular activity. The phosphonium salts were synthesized through a 1, 3-dipolar cycloaddition (click) reaction. The structures of all synthesized compounds were elucidated using ^{1}H NMR, ^{13}C NMR, AT-FTIR, and HR-LCMS spectroscopy. The compounds were screened for antitubercular activity against *Mycobacterium tuberculosis* H37Rv and multidrug-resistant TB (MDR-TB) with Rifampicin and Isoniazid, Notably, derivatives **1d** and **1e** demonstrated the most potent activity, achieving 100 % inhibition of MDR-TB at a minimum inhibitory concentration (MIC) of 6.25 μg/mL. At 100 μg/mL, these compounds reduced the colony-forming units (CFU) of MDR-TB by 96 % and 64 %, respectively. Compounds **2e, 3e,** and **3f** also displayed inhibitory activity against H37Rv, with **2e** showing moderate efficacy (68 % inhibition, 6.25 μg/mL) towards MDR-TB and the highest selectivity index against murine macrophages. Molecular docking studies against seventeen (17) *M. tuberculosis* target proteins revealed that compounds **1d**, **1e**, and **2e** displayed the strongest binding affinity for InhA (PDB ID: 5MTP), a key enzyme in mycolic acid biosynthesis, interacting critically with residues TYR158, PHE149, MET199, ILE194, and SER94. MM/GBSA calculations further confirmed the favorable binding free energies of these complexes. All compounds exhibited favorable predicted oral bioavailability and drug-like properties. These findings highlight the click-tethered phosphonium salts, particularly **1d**, as promising lead candidates for the development of novel antitubercular agents targeting InhA through a mechanism of dynamic stabilization.

1. Introduction

Tropical infectious diseases continue to create significant global health crises because of their devastating effects, which include causing several million deaths each year and accounting for more than 25 % of the global disease burden [1,2]. Although considerable efforts have been put in place through public education, stakeholder partnership, and various treatment options, the situation has only been marginally improved [3,4]. WHO priority disease, tuberculosis (TB), caused by the bacillus *Mycobacterium tuberculosis* is an infectious disease with public health implications and a high mortality rate of 1.2 million people globally in 2023 [5]. TB is one of the major airborne infectious diseases associated with an estimated 9 million new cases and 2 million deaths annually, with over 85 % of these deaths occurring in low- and middle-income countries due to a lack of proper education on the disease and healthcare infrastructure [6,7]. Studies suggest that about one-third of the world's population has latent tuberculosis and that 5–15 % will develop active tuberculosis in their lifetime, with immunocompromised persons being at a higher risk [8] [9]. The World Health Organization (WHO) rated TB as the world's most infectious disease worldwide. TB

* Corresponding author at: Department of Pharmaceutical Chemistry, School of Pharmacy, University of Health and Allied Sciences, Ho, Ghana
E-mail address: camengor@uhas.edu.gh (C.D.K. Amengor).

https://doi.org/10.1016/j.bioorg.2025.109390
Received 11 October 2025; Received in revised form 7 December 2025; Accepted 14 December 2025
Available online 19 December 2025

serves as the most infectious disease globally, alongside HIV/AIDS, with the estimated number of patients increasing to 0.8 million in 2023 [10,11]. A more alarming incident is the resurgence of 10 % cases of extensively drug-resistant tuberculosis (XDR-TB) in Ghana in March 2018. These strains of multi-drug-resistant TB are not susceptible to fluorinated quinolones and the second-line parenteral [12,13]. This unusual resistance to TB drugs is partly associated with the most significant tool of *Mycobacterium,* which is the unusually thick biological membrane impregnated with mycolic acids interspersed with polysaccharides, making it hydrophobic to prevent desiccation and also serving as a barricade to most drugs. Also, over time, the development of built-in resistance genes and efflux pumps adds to the resistant strains of this Gram-positive bacilli [14,15].

TB has been treated previously with some medications, including heavy metals, herbs and currently with a four-drug combination comprising isoniazid (Fig. 1a), ethambutol (Fig. 1b), pyrazinamide (Fig. 1c), and rifampicin (Fig. 1**d**) as a first-line dosage regimen by employing Directly Observed Therapy (DOTs), but no lasting solution has been achieved [16,17].

With the global threat of resistance to current chemotherapy, toxicity, and some pharmacokinetic issues, this research describes the **design, synthesis, computational evaluation, and biological assessment** of a novel series of **1,2,3-triazole "clicked" derivatives and their corresponding phosphonium salts**. Drug discovery has greatly focused on 1, 2, 3-triazoles due to their excellent metabolic stability and versatile biological properties [18,19]. In recent times, 1, 4-disubstituted 1, 2, 3-triazoles have inhibited avirulent MTB H3R7v, including their chlorinated heterocyclic series of compounds with MICs ranging from 0.62 to 25 μg/mL (Fig. 2a-2c) [20–22].

2a: MIC = 25 μg/mL 2b: MIC = 2 μg/mL 2c: MIC = 0.62 μg/mL.

The synthesis of the 1, 2, 3-triazoles is usually catalyzed by Cu(I) to yield regioselective 1,4-disubstituted triazoles, which is an advantage over the non-selective Huisgen azide-alkyne 1,3-dipolar cycloaddition captured in click chemistry reactions [23–25].

On the other hand, a small, focused library of triazoles with varying substituents exhibited broad-spectrum activity against a panel of bacteria, including *Mycobacterium tuberculosis.* From their SAR, studies have shown that the nature of the varying substituents can have a significant contribution to their antimicrobial activity, with more than 85 % of FDA-registered drugs containing the heterocyclic triazole. Quartenary salts including phosphonium salts are also known to exhibit versatile antimicrobial potential including antitubercular activity [26,27]. Following up on earlier reports by the research group and encouraged by these achievements of 1,4-disubstituted 1,2,3-triazoles and phosphonium salts, the overall proposed molecule for this study is made up of two covalently linked bioactive groups (substituted aromatic and lipophilic phosphonium cation) as a single hybrid entity. This would be achieved by employing the versatile 1,2,3-triazole nucleus (biologically active) as a linker, herein referred to as pharmacophore hybridization into a molecular framework, a common drug design approach to improve potency, ADME profile, and reduce treatment duration.

2. Experimental section

2.1. Chemistry

The starting materials used for the synthesis were purchased from Merck ® (Gillingham, United Kingdom) and were of analytical grade except for the HPLC-grade solvents (methanol and acetonitrile) used for the HR LCMS analysis. The reaction progress and purity of the intermediate and final synthesized compounds were monitored by thin-layer chromatography using aluminium plates pre-coated with silica gel with F_{254} at a detection wavelength of 254 nm. Synthesized compounds were characterised by thin-layer chromatography (TLC), melting points (B-540 melting point analyzer (Büchi Corporation, New Castle, DE, USA), infra-red spectroscopy (FTIR spectrophotometer 41,000 ExoScan, Agilent Technologies, U.S.A.), NMR spectroscopy (Bruker BioSpin AG Avance III ™ HD X 500 MHz (Germany) and High-resolution mass spectra (Shimadzu LC-2010 A) in tandem with a time-of-flight (quadrupole mass analyzer) in a positive ESI ionization mode. The methods for the synthetic schemes were adapted from Amengor and co-workers 2022, which captures **compounds 2a** and **3a** in this study [28].

2.1.1. 1-(azidomethyl)-4-nitrobenzene (1)

Yield: (1.483 g, 83 %) as a deep yellow oil (R_f 0.82, Petroleum ether: EtOAc (90:10). ^{1}H NMR (500 MHz, $CDCl_3$, room temperature) δ 8.20 (2H, d, J = 8.5, C(4)H, C(6)H), 7.50 (2H, d, J = 8.5 Hz, C(3)H, C(7)H), 4.51 (2H, s, C(1)H_2) was consistent with literature data [29].

2.1.2. 1-(azidomethyl)-3-nitrobenzene (2).

Yield (1.731 g, 97 %) as a deep yellow oil (R_f 0.78, Petroleum ether: EtOAc (90:10). ^{1}H NMR (500 MHz, $CDCl_3$, room temperature) δ 8.04 (1H, m, C(4)H), 7.81 (1H, m, C(2)H), 7.60 (1H, m, C(5)H) 4.51 (2H, s, C (1)H2) were consistent with literature data [29].

2.1.3. 1-(azidomethyl)-2-nitrobenzene (3).

Yield (1.570 g, 88 %) as a deep yellow oil (R_f 0.80, Petroleum ether: EtOAc (90:10). ^{1}H NMR (500 MHz, $CDCl_3$, room temperature) δ 7.91 (1H, m, C(3)H), 7.50 (1H, m, C(4)H), 7.64 (1H, m, C(5)H), 7.42 (1H, m, C(6)H), 4.51 (2H, s, C(1)H2) was consistent with literature data [30] (Diesendruck et al., 2014).

2.1.4. 1-(azidomethyl)-4-chlorobenzene (4).

Yield (1.600 g, 96 %) as a colourless oil (R_f 0.62, Petroleum ether: EtOAc (90:10). ^{1}H NMR (500 MHz, $CDCl_3$, room temperature) δ 7.30 (2H, d, J = 8.5, C(4)H, C(6)H), 7.10 (2H, d, J = 8.5 Hz, C(3)H, C(7)H), 2.70 (2H, s, C(1)H_2).

2.1.5. 1-(azidomethyl)-3-chlorobenzene (5).

Yield (1.250 g, 75 %) as a colourless oil ((R_f 0.56, Petroleum ether: EtOAc (90:10). ^{1}H NMR (500 MHz, $CDCl_3$, room temperature) δ 7.34 (1H, m, C(3)H)), 7.18 (1H, m, C(4)H), 7.13 (1H, m, C(5)H), 7.12 (1H, m, C(6)H), 2.71 (2H, s, C(1)H_2).

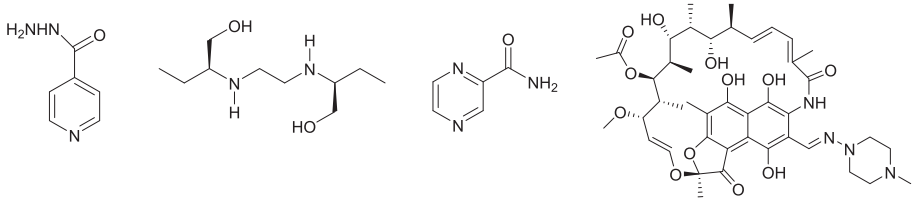

Fig. 1. Chemical structures of first-line antitubercular drugs.

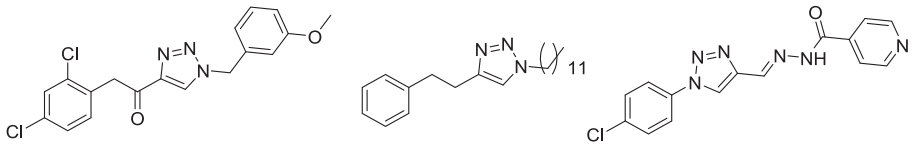

Fig. 2. Triazoles with antitubercular activity against MTB avirulent strain H37Rv.

2.1.6. 1-(azidomethyl)-2-chlorobenzene (6).

Yield (1.4300 g, 86 %) as a colourless oil (R_f 0.63, Petroleum ether: EtOAc (90:10). ^{1}H NMR (500 MHz, $CDCl_3$, room temperature) δ 7.54 (2H, m, C(3)H)), 7.30 (1H,m, C(2)H), 7.12 (1H,m, C(5)H), 2.71 (2H, s, C $(1)H_2$).

2.1.7. (2-(1-(4-nitrobenzyl)-1H-1, 2,3-triazol-4-yl)phenyl)methanol (7)

Yield: (1.190 g, 74 %) as a white solid. (R_f 0.23, EtOAc, Et_3N 9.5:5). mp 134–136 °C; IR ν_{max}/cm^{-1}: 3311(O—H), 3130 (C=**C-H**), 2981 (sp^3 C—H); ^{1}H NMR (500 MHz, DMSO-d_6, room temperature) δ_H 8.12–8.15 (2H, d, J = 8.0, C(8)H_{Ar}, C(10)H_{Ar}), 7.75 (1H, s, C(5)$H_{triazole}$), 7.68 (2H, d, J = 8.0, C(7)H_{Ar}, C(11)H_{Ar}), 7.32–7.37 (4H, dd, J = 25.0, 9.0, C(12) H_{Ar}), C(13)H_{Ar}), C(15) H_{Ar}, (16)H_{Ar}), 5.60 (2H, s, C(1^1)H_2), 4.58 (2H, d, J = 6.0, C(2^1)H_2) 3.82 (1H, t, J = 6.0, C(2^1)-OH); ^{13}C (500 MHz, DMSO-d_6, room temperature): δ_C 147.9, 147.5, 143.9, 142.9, 129.5, 127.5, 125.5, 124.6, 122.4 (Ar) 63.0, 52.7; HRMS (ESI): *m/z* calculated for $[M + H]^+$ $C_{11}H_{11}N_3O_3$, 311.1144, found 311.1158.

2.1.8. 2-(1-(3-nitrobenzyl)-1H-1,2, 3-triazol-4-yl)phenyl)methanol (8).

Yield: (1.200 g, 80 %) as a white solid, (R_f 0.23, EtOAc, Et_3N 9.5:5). mp 143–144 °C; IR ν_{max}/cm^{-1}: 3311(O—H), 3130 (C=**C-H**), 2981 (sp^3 C—H); ^{1}H NMR (500 MHz, DMSO-d_6, room temperature): δ_H 8.65 (1H, s, C(5)$H_{triazole}$), 8.21–8.30 (2H, m, C(9)H_{Ar}, C(11)H_{Ar}), 7.78–7.81 (3H, m, H_{Ar}), 7.68–7.70 (1H, m, H_{Ar}), 7.35–7.40 (2H, d, J = 10.0, H_{Ar}), (2H, s, C(1^1)H_2), 5.22 (1H, t, J = 7.5, C(2^1)-OH), 4.50 (2H, d, J = 7.5, C(1^1)H_2); ^{13}C (500 MHz, DMSO-d_6, room temperature): δ_C 148.3147.1143.2, 139.2, 138.4127.5, 125.5123.7, 122.1 (Ar) 63.2, 52.5; HRMS (ESI): *m/z* calculated for $[M + H]^+$ $C_{16}H_{14}N_3O_3$, 311.1144, found 311.1151.

2.1.9. 2-(1-(2-nitrobenzyl)-1H-1, 2,3-triazol-4-yl)phenyl)methanol (9)

Yield: (1.300 g, 87 %) as a white solid, (R_f 0.25, EtOAc, Et_3N 9.5:5). mp 172–173 °C; IR ν_{max}/cm^{-1}: 3300 (O—H), 3010 (C=**C-H**), 2981 (sp^3 C—H); ^{1}H NMR (500 MHz, DMSO-d_6, room temperature): δ_H 8.55 (1H, s, C(5)$H_{triazole}$), 8.11–8.15 (2H, d, J = 9.0, C(10)H_{Ar}, C(7)H_{Ar}) 7.11–7.15 (2H, m, H_{Ar}, C(8)H_{Ar}, C(11)H_{Ar}), 7.34–7.37 (4H, m, C(12)H_{Ar}), C(13) H_{Ar}, C(15)H_{Ar}, C(16)H_{Ar}), 7.15 (2H, d, J = 9.0, C(8)H), C(9)H), 5.98 (2H, s, C(1^1)H_2), 5.20 (1H, t, J = 5.0, C(2^1)-OH), 4.50 (2H, t, J = 5.0, C (2^1)H_2); ^{13}C (500 MHz, DMSO-d_6, room temperature): δ_C 148.5, 147.5, 143.0, 135.0, 131.3, 127.5, 125.8, 125.6, 122.6 (Ar), 63.0, 51.0; HRMS (ESI): *m/z* calculated for $[M + H]^+$ $C_{16}H_{14}N_3O_3$, 311.1144, found 311.1154.

2.1.10. 2-(1-(4-chlorobenzyl)-1H-1, 2, 3-triazol-4-yl) phenyl) methanol (10)

Yield: (1.270 g, 85 %) as a white solid, (R_f 0.28, EtOAc, Et_3N 9.5:5). mp 140–142 °C; IR ν_{max}/cm^{-1}**:** 3313 (O—H), 3131 (C=C-H), 2981 (C—H); ^{1}H NMR (500 MHz, DMSO-d_6, room temperature): δ_H 8.63 (1H, s, C(5)H), 7.79–7.82 (2H, m, C(9)H_{Ar}, C(11)H_{Ar}), 7.36–7.47 (6H, m, H_{Ar}), 5.70 (2H, s, C(1^1)H_2), 5.20 (1H, t, J = 7.0, C(2^1)-OH), 4.50 (2H, d, J = 7.0, C(2^1)H_2); ^{13}C (500 MHz, DMSO-d_6, room temperature): δ_C 147.5, 142.9, 133.9, 131.3, 129.7, 125.8, 125.5, 121.9 (Ar), 63.3, 52.9; HRMS (ESI): *m/z* calculated for $[M + H]^+$ $C_{16}H_{15}N_3O^{35}Cl$, 300.0904, found, 300.0904. Calculated for $[M + H]^+$ $C_{16}H_{15}N_3O^{37}Cl$, 302.0904, found, 300.0878.

2.1.11. 2-(1-(3-chlorobenzyl)-1H-1, 2, 3-triazol-4-yl) phenyl) methanol (11)

Yield: (1.225 g, 87 %) as a white solid, (R_f 0.28, EtOAc, Et_3N 9.5:5). mp 140–142 °C; IR ν_{max}/cm^{-1}**:** 3313 (O—H), 3131 (C=C-H), 2981 (C—H); ^{1}H NMR (500 MHz, DMSO-d_6, room temperature): δ_H 8.65 (1H, s, C(5)$H_{triazole}$), 8.21–8.30 (2H, m, C(9)H_{Ar}, C(11)H_{Ar}), 7.78–7.81 (3H, m, H_{Ar}), 7.68–7.70 (1H, m, H_{Ar}), 7.35–7.40 (2H, d, J = 10.0, H_{Ar}), (2H, s, C(1^1)H_2), 5.22 (1H, t, J = 7.5, C(2^1)-OH), 4.50 (2H, d, J = 7.5, C(1^1)H_2); ^{13}C (500 MHz, DMSO-d_6, room temperature): δ_C 148.3147.1143.2, 139.2, 138.4127.5, 125.5123.7, 122.1 (Ar) 63.2, 52.5; HRMS (ESI): *m/z* calculated for $[M + H]^+$ $C_{16}H_{14}N_3O_3$, 311.1144, found 311.1151.

2.1.12. 2-(1-(2-chlorobenzyl)-1H-1, 2, 3-triazol-4-yl) phenyl) methanol (12)

Yield: (1.300 g, 87 %) as a white solid (R_f 0.28, EtOAc, Et_3N 9.5:5). mp 140–142 °C; IR ν_{max}/cm^{-1}**:** 3313 (O—H), 3131 (C=C-H), 2981 (C—H); ^{1}H NMR (500 MHz, DMSO-d_6, room temperature): δ_H 8.55 (1H, s, C(5)H), 8.11–8.15 (2H, d, J = 9.0, C(10)H_{Ar}, C(7)H_{Ar}) 7.11–7.15 (2H, m, H_{Ar}, C(8)H_{Ar}, C(11)H_{Ar}), 7.34–7.37 (4H, m, C(12)H_{Ar}), C(13)H_{Ar}, C (15)H_{Ar}, C(16)H_{Ar}), 7.15 (2H, d, J = 9.0, C(8)H), C(9)H), 5.98 (2H, s, C (1^1)H_2), 5.20 (1H, t, J = 5.0, C(2^1)-OH), 4.50 (2H, t, J = 5.0, C(2^1)H_2); ^{13}C (500 MHz, DMSO-d_6, room temperature): δ_C 148.5, 147.5, 143.0, 135.0, 131.3, 127.5, 125.8, 125.6, 122.6 (Ar), 63.0, 51.0; HRMS (ESI): *m/z* calculated for $[M + H]^+$ $C_{16}H_{14}N_3O_3$, 311.1144, found 311.1154.

2.1.13. 4-(2-(bromomethyl) phenyl)-1-(4-nitrobenzyl)-1H-1, 2, 3-triazole (13)

Yield: (0.178 g, 96 %) as a white solid, (R_f 0.67, hexane, EtOAc 6:4). mp 156–158; IR ν_{max}/cm^{-1}: 3130 (C=C-H), 2981 (sp^3 C—H), 1515 (N—H); ^{1}H NMR (500 MHz, DMSO-d_6, room temperature): δ_H 8.68 (1H, s, C(5)$H_{triazole}$), 8.21–8.23 (2H, d, J = 9.0, C(8)H_{Ar}, C(10) H_{Ar}), 7.80–7.82 (2H, d, J = 9.0, C(9)H_{Ar}, C(11)H_{Ar}), 7.53–7.55 (2H, d, J = 9.0, C(13) H_{Ar}, C(15)H_{Ar}), 7.48–7.49 (2H, d, J = 9.0, C(12)H_{Ar}, C(16)H_{Ar}), 5.81 (2H, s, C(1^1)H_2), 4.70 (2H, s, C(2^1)H_2).; ^{13}C (500 MHz, DMSO-d_6, room temperature) 148.7, 146.7, 138.4, 135.3, 131.0, 130.5, 126.2, 123.7, 123.4, 122.7, (Ar), 52.5, 34.9; HRMS (ESI): *m/z* calculated for $[M]^+$ $C_{16}H^{79}_{13}BrN_4O_2$, 373.0300, found 373.0301. $[M]^+$ $C_{16}H^{81}_{13}BrN_4O_2$, 375.0300, found 373.0277.

2.1.14. 3-(4-(bromomethyl)phenyl)-1-(3-nitrobenzyl)-1H-1,2,3-triazole (14)

Yield: (0.851 g, 65 %) as a white solid, (R_f 0.67, hexane, EtOAc 6:4). mp 135–136 °C; IR ν_{max}/cm^{-1}: 3130 (C=**C-H**), 2981 (sp^3 C—H),1515 (N—H); ^{1}H NMR (500 MHz, DMSO-room temperature): δ_H 8.72 (1H, s, C (5)$H_{triazole}$), 8.21–8.29 (2H, m, C(9)H_{Ar}), C(11)H_{Ar}), 7.80–7.85 (3H, m, H_{Ar}), 7.73 (1H, m, H_{Ar}), 7.50–7.55 (2H, m, H_{Ar}), 5.84 (2H, s, C(1^1)H_2), 4.74 (2H, s, C(2^1)H_2); ^{13}C (500 MHz, DMSO-d_6) δ_C 148.2, 146.8, 138.1, 135.0, 131.2, 130.8, 126.0, 125.7, 123.4, 123.1 (Ar), 51.6, 34.5; HRMS (ESI): *m/z* calculated for $[M]^+$ $C_{16}H^{79}_{13}BrN_4O_2$, 373.0300, found 373.0299. Calculated for $[M]^+$ $C_{16}H^{81}_{13}BrN_4O_2$, 375.0300, found 373.0277.

2.1.15. 2-(4-(bromomethyl) phenyl)-1-(2-nitrobenzyl)-1H-1,2,3-triazole (15).

Yield: (0.921 g, 75 %) as a white solid, (R_f 0.70, hexane, EtOAc 6:4). mp 177–179 °C; IR v_{max}/cm^{-1}: 3130 (C=**C-H**), 2981 (sp^3 C—H), 1517 (N—H); ^1H NMR (500 MHz, DMSO-d_6, room temperature): δ_H 8.64 (1H, s, C(5)$H_{triazole}$), 8.16–8.19 (1H, dd, J = 10.0, 10.0, H_{Ar}), 7.50–7.95 (6H, m, H_{Ar}), 7.16–7.19 (1H, m, H_{Ar}), 6.03 (2H, s, C(1^1)H_2), 4.74 (2H, s, C(2^1)H); ^{13}C (500 MHz, DMSO-d_6, room temperature) δ_C 148.7, 146.7, 138.4, 135.3, 131.0, 130.5, 126.2, 123.7, 123.4, 122.7 (Ar), 52.5, 34.9; HRMS (ESI): *m/z* calculated for $[M]^+$ $C_{16}H_{13}^{79}BrN_4O_2$, 373.0300, found 373.0298. Calculated $[M]^+$ $C_{16}H_{13}^{81}BrN_4O_2$, 375.0300, found 373.0280.

2.1.16. 4-(2-(bromomethyl) phenyl)-1-(4-chlorobenzyl)-1H-1,2,3-triazole (16)

Yield: (1.400 g, 78 %) as a white solid (R_f 0.50, hexane, EtOAc 6:4). mp 146–149 °C; IR v_{max}/cm^{-}1: 3130 (C=C-H), 2981 (sp^3 C—H),1576 (N—H); ^1H NMR (500 MHz, DMSO-d_6) δ_H 8.69 (1H, s, C(5)$H_{triazole}$), 7.83–7.86 (2H, d, J = 10.5, H_{Ar}), 7.40–7.55 (6H, m, H_{Ar}), 5.68 (2H, s, C(1^1)H_2, 4.74 (2H, s, C(2^1)H_2); ^{13}C (500 MHz, DMSO-d_6) δ_C 147.3, 142.8, 138.9, 133.6, 131.4, 129.5, 128.7, 128.4, 127.4, 127.2, 125.5, 121.9 (Ar), 63.2, 52.8; HRMS (ESI): *m/z* calculated for $[M]^+$ $C_{16}H_{13}^{79}Br^{35}ClN_3$, 362.0060, found 362.0540. Calculated for $[M]^+$ $C_{16}H_{13}^{79}Br^{37}ClN_3$, 364.0060, found 364.000. Calculated for $[M]^+$ $C_{16}H_{13}^{81}Br^{35}ClN_3$, 364.0600, found 364.0034. Calculated for $[M]^+$ $C_{16}H_{13}^{81}Br^{37}ClN_3$, 366.0060, found 366.0000.

2.1.17. 4-(2-(bromomethyl) phenyl)-1-(3-chlorobenzyl)-1H-1,2,3-triazole (17)

Yield (1.370 g, 76 %) as a white solid, (R_f 0.50, hexane, EtOAc 6:4). mp 146–149 °C; IR v_{max}/cm^{-}1: 3130 (C=**C-H**), 2981 (sp^3 C—H),1576 (N—H); ^1H NMR (500 MHz, DMSO-d_6) δ_H δ_H 8.72 (1H, s, C(5)$H_{triazole}$), 8.21–8.29 (2H, m, C(9)H_{Ar}), C(11)H_{Ar}), 7.80–7.85 (3H, m, H_{Ar}), 7.73 (1H, m, H_{Ar}), 7.50–7.55 (2H, m, H_{Ar}), 5.84 (2H, s, C(1^1)H_2), 4.74 (2H, s, C(2^1)H_2); ^{13}C (500 MHz, DMSO-d_6) δ_C 148.2, 146.8, 138.1, 135.0, 131.2, 130.8, 126.0, 125.7, 123.4, 123.1 (Ar), 51.6, 34.5; HRMS (ESI): *m/z* calculated for $[M]^+$ $C_{16}H_{13}^{79}BrN_4O_2$, 373.0300, found 373.0299. Calculated for $[M]^+$ $C_{16}H_{13}^{81}BrN_4O_2$, 375.0300, found 373.0277.

2.1.18. 4-(2-(bromomethyl) phenyl)-1-(2-chlorobenzyl)-1H-1,2, 3-triazole (18).

Yield: (1.3850 g, 78 %) as a white solid, (R_f 0.50, hexane, EtOAc 6:4). mp 146–149 °C; IR v_{max}/cm^{-}1: 3130 (C=**C-H**), 2981 (sp^3 C—H),1576 (N—H); ^1H NMR (500 MHz, DMSO-d_6) δ_H 8.64 (1H, s, C(5)$H_{triazole}$), 8.16–8.19 (1H, dd, J = 10.0, 10.0, H_{Ar}), 7.50–7.95 (6H, m, H_{Ar}), 7.16–7.19 (1H, m, H_{Ar}), 6.03 (2H, s, C(1^1)H_2), 4.74 (2H, s, C(2^1)H); ^{13}C (500 MHz, DMSO-d_6, room temperature) δ_C 148.7, 146.7, 138.4, 135.3, 131.0, 130.5, 126.2, 123.7, 123.4, 122.7 (Ar), 52.5, 34.9; HRMS (ESI): *m/z* calculated for $[M]^+$ $C_{16}H_{13}^{79}BrN_4O_2$, 373.0300, found 373.0298. Calculated $[M]^+$ $C_{16}H_{13}^{81}BrN_4O_2$, 375.0300, found 373.0280.

2.1.19. (2-(1-(4-nitrobenzyl)-1H-1, 2, 3-triazol-4-yl) benzyl) triphenylphosphonium bromide (1a).

Yield (0.064 g, 78 %) as a white solid. mp 289–290 °C; IR v_{max}/cm^{-1}: 2873 (sp^3 C—H) 1605, 1517, 507 (ArC-H), 565–450 (Ar-P-C); ^1H NMR (500 MHz, DMSO-d_6, room temperature): δ_H 8.63 (1H, s, C(5)$H_{triazole}$), 8.20 (2H, d, J = 8.5, H_{Ar}), 7.86–7.90 (3H, t, J = 8.5, H_{Ar}), 7.62–7.76 (15H, m, H_{ArP}), 7.50–7.55 (2H, d, J = 8.5, H_{Ar}), 6.90–7.02 (2H, dd, J = 8.0, 8.5, H_{Ar}), 5.80 (2H, s, C(1^1)H), 5.17 (2H, d, J = 16.0, C(2^1)H_2); ^{13}C (500 MHz, DMSO-d_6, room temperature) δ_C 147.9, 146.5, 143.9, 135.7, 134.8, 132.0, 130.8, 130.7, 129.6, 128.1, 125.9, 124.6, 128.8, 122.9, 118.7, 117.9, 52.9C(2^1); HRMS (ESI): *m/z* calculated for $[M\text{-}HBr]^+$ $C_{34}H_{28}N_4O_2P^+$, 555.1940, found 555.1930.

2.1.20. (2-(1-(3-nitrobenzyl)-1H-1, 2, 3-triazol-4-yl) benzyl) triphenylphosphonium bromide (1b).

Yield: (0.070 g, 85 %) as a white solid. mp 246–249 °C; IR v_{max}/cm^{-1}: 2866 (sp^3 C—H) 1588, 1531, 722 (Ar C—H), 565–450 (Ar-P-C); ^1H NMR (500 MHz, DMSO-d_6, room temperature): δ_H 8.58 (1H, s, C(5)$H_{triazole}$), 8.16–8.18 (1H, m, H_{Ar}), 7.90–7.95 (3H, m, J = 10.5, H_{Ar}), 7.60–7.80 (15H, m, H_{ArP}), 7.21 (1H, d, J = 10.5, H_{Ar}), 7.01–7.05 (2H, dd, J = 10.5, 10.5, H_{Ar}), 6.00 (2H, s, C(1^1)H_2), 5.15–5.20 (2H, d, J = 20.0, C(2^1)H_2); ^{13}C (500 MHz, DMSO-d_6, room temperature) δ_C 148.5, 135.7, 134.5, 131.9, 130.7, 130.6, 125.9, 123.8, 123.4, 122.7, 118.7, 117.8 (Ar), 52.6; HRMS (ESI): *m/z* calculated for $[M\text{-}HBr]^+$ $C_{34}H_{28}N_4O_2P^+$, 555.1950, found 555.1953.

2.1.21. (2-(1-(2-nitrobenzyl)-1H-1, 2, 3-triazol-4-yl) benzyl) triphenylphosphonium bromide (1c).

Yield: (0.060 g, 73 %) as a white solid. mp 277–280 °C; IR v_{max}/cm^{-1}: 2982 (sp^3 C—H) 1589, 1526, 508 (Ar C=C-H), 565–450 (Ar-P-C); ^1H NMR (500 MHz, DMSO-d_6, room temperature): δ_H 8.00 (1H, s, C(5)$H_{triazole}$), 7.62–7.64 (1H, dd, J = 8.0, 8.0, H_{Ar}), 7.38 (3H, m, H_{Ar}), 7.10–7.24 (15H, m, H_{ArP}), 6.66–6.68 (1H, m, H_{Ar}), 6.48–6.52 (2H, m, H_{Ar}), 5.45 (2H, s, C(1^1)H_2), 4.61–4.67 (2H, d, J = 16.0, C(2^1)H_2); ^{13}C (500 MHz, DMSO-d_6, room temperature) δ_C 138.0, 137.9, 132.9, 131.9, 129.6, 126.2, 124.5, 122.9, 118.2, 118.5 (Ar), 52.6; HRMS (ESI): *m/z* calculated for $[M\text{-}HBr]^+$ $C_{34}H_{28}N_4O_2P^+$, 555.1950, found 555.1957.

2.1.22. (2-(1-(4-chlorobenzyl)-1H-1, 2, 3-triazol-4-yl)benzyl)triphenyl-phosphonium bromide (1d).

Yield (0.068 g, 75 %) as a white solid. mp 297–300 °C; IR v_{max}/cm^{-1}: 3056 (sp^3 C—H) 1602, 1576, 850 (Ar C=C-H), 565–450 (ArP-C); ^1H NMR (500 MHz, DMSO-d_6, room temperature): δ_H 8.58 (1H, s, C(5)$H_{triazole}$), 7.84–7.90 (3H, m, H_{Ar}), 7.60–7.75 (15H, m, H_{ArP}), 7.38–7.41 (2H, m, H_{Ar}), 7.25–7.27 (1H, m, H_{Ar}), 6.97–7.00 (2H, m, H_{Ar}), 5.62 (2H, s, C(1^1)H_2), 5.12–5.16 (2H, d, J = 16.0, C(2^1)H_2); ^{13}C (500 MHz, DMSO-d_6, room temperature) δ_C 135.7, 134.6, 134.3, 131.9, 131.3, 130.7, 128.5, 127.4, 125.9, 122.6, 118.7, 117.7 (Ar), 52.8; HRMS (ESI): *m/z* calculated for $[M\text{-}HBr]^+$ $C_{34}H_{28}N_3^{35}ClP^+$, 544.1705, found 544.1705. Calculated for $[M\text{-}HBr^+$ $C_{34}H_{28}N_3^{37}ClP^+$, 546.1705, found 546.1691.

2.1.23. (2-(1-(3-chlorobenzyl)-1H-1, 2,3-triazol-4-yl)benzyl)triphenyl-phosphonium bromide (1e).

Yield: (0.052 g, 70 %) as a white solid. mp 292–295 °C; IR v_{max}/cm^{-1}: 3056 (sp^3 C—H) 1602, 1576, 850 (Ar C=C-H), 565–450 (ArP-C); ^1H NMR (500 MHz, DMSO-d_6, room temperature): δ_H 8.58 (1H, s, C(5)$H_{triazole}$), 7.84–7.90 (3H, m, H_{Ar}), 7.60–7.75 (15H, m, H_{ArP}), 7.38–7.41 (2H, m, H_{Ar}), 7.25–7.27 (1H, m, H_{Ar}), 6.97–7.00 (2H, m, H_{Ar}), 5.62 (2H, s, C(1^1)H_2), 5.12–5.16 (2H, d, J = 16.0, C(2^1)H_2; ^{13}C (500 MHz, DMSO-d_6, room temperature) δ_C 135.7, 134.6, 134.3, 131.9, 131.3, 130.7, 128.5, 127.4, 125.9, 122.6, 118.7, 117.7 (Ar), 52.8; HRMS (ESI): *m/z* calculated for $[M\text{-}HBr]^+$ $C_{34}H_{28}N_3^{35}ClP^+$, 544.1705, found 544.1705. Calculated for $[M\text{-}HBr^+$ $C_{34}H_{28}N_3^{37}ClP^+$, 546.1705, found 546.1691.

2.1.24. (2-(1-(2-chlorobenzyl)-1H-1, 2,3-triazol-4-yl)benzyl)triphenyl-phosphonium bromide (1f).

Yield: (0.050 g, 68 %) as a white solid. mp 287–290 °C; IR v_{max}/cm^{-1}: 3056 (sp^3 C—H) 1602, 1576, 850 (Ar C=C-H), 565–450 (ArP-C); ^1H NMR (500 MHz, DMSO-d_6, room temperature): δ_H 8.58 (1H, s, C(5)$H_{triazole}$), 7.84–7.90 (3H, m, H_{Ar}), 7.60–7.75 (15H, m, H_{ArP}), 7.38–7.41 (2H, m, H_{Ar}), 7.25–7.27 (1H, m, H_{Ar}), 6.97–7.00 (2H, m, H_{Ar}), 5.62 (2H, s, C(1^1)H_2), 5.12–5.16 (2H, d, J = 16.0, C(2^1)H_2); ^{13}C (500 MHz, DMSO-d_6, room temperature) δ_C 135.7, 134.6, 134.3, 131.9, 131.3, 130.7, 128.5, 127.4, 125.9, 122.6, 118.7, 117.7 (Ar), 52.8; HRMS (ESI): *m/z* calculated for $[M\text{-}HBr]^+$ $C_{34}H_{28}N_3^{35}ClP^+$, 544.1705, found 544.1705. Calculated for $[M\text{-}HBr^+$ $C_{34}H_{28}N_3^{37}ClP^+$, 546.1705, found 546.1691.

2.1.25. (2-(1-benzyl-1H-1, 2,3-triazol-4-yl)benzyl)triphenylphosphonium bromide (1 g).

Yield: (0.035 g, 60 %) as a white solid. mp 278–281 °C; IR v_{max}/cm^{-1}: 2864 (sp^3 C—H) 1588, 1528, 851 (Ar C=C-H), 565–450 (Ar-P-C); ^{1}H NMR (500 MHz, DMSO-d_6, room temperature): δ_H 8.56 (1H, s, C(5) $H_{triazole}$), 7.85–7.90 (3H, m, H_{Ar}), 7.60–7.75 (15H, m, H_{ArP}), 7.27–7.39 (4H, m, H_{Ar}), 6.90–7.01 (2H, dd, J = 10.0, 10.0, Ar—H), 5.57–5.59 (2H, s, C(1^1)H_2), 5.10–5.17 (2H, d, J = 20.0, C(2^1)H_2);; ^{13}C (500 MHz, DMSO-d_6, room temperature) δ_C 145.9, 136.1, 135.2, 134.0, 131.3, 130.7, 129.1, 128.2, 125.4, 122.2, 118.1, 117.5, 53.0; HRMS (ESI): *m/z* calculated for $[M\text{-}HBr]^+$ $C_{34}H_{29}N_3P^+$, 510.2099, found 510.2095.

2.1.26. 2-(1-(4-(nitrobenzyl)-1H-1, 2, 3-triazol-4-yl) benzyl)tri-p-tolylphosphonium bromide (2a).

Yield: (0.250 g, 74 %) as a white solid. mp 316–319 °C. IR v_{max}/cm^{-1}: 3023 (sp^3 C—H) 1599, 1517, 860 (Ar C=C-H), 565–450 (Ar-P-C); ^{1}H NMR (500 MHz, DMSO-d_6, room temperature): δ_H 8.66 (1H, s, C(5) $H_{triazole}$), 8.24–8.27 (2H, d, J = 10.5, H_{Ar}), 7.40–7.60 (14H, m, H_{Ar}), 7.01–7.06 (2H, m, H_{Ar}), 5.84 (2H, s, C(1^1)H_2), 5.04–5.10 (2H, d, J = 20.0, C(2^1)H_2); 2.45 (9H, s, $H_{Ar}CH_3$); ^{13}C (500 MHz, DMSO-d_6, room temperature) δ_C 148.3, 146.2, 144.2, 134.5, 131.9, 131.2, 130.0, 125.9, 124.3, 122.8, 115.9, 114.7 (Ar), 52.1, 21.8; HRMS (ESI): *m/z* calculated for $[M\text{-}HBr]^+$ $C_{36}H_{32}N_4O_2P^+$, 597.2373, found 597.2374.

2.1.27. (2-(1-(3-nitrobenzyl)-1H-1, 2, 3-triazol-4-yl) benzyl)tri-p-tolyl phosphonium bromide (2b)

Yield: (0.270 g, 80 %) as a white solid. mp 280–283 °C; IR v_{max}/cm^{-1}: 2980 (sp^3 C—H) 1598, 1530, 857 (Ar C=C-H), 565–450 (Ar-P-C); ^{1}H NMR (500 MHz, DMSO-d_6, room temperature): δ_H 8.65 (1H, s, C(5) $H_{triazole}$), 8.21–8.26 (2H, m, H_{Ar}), 7.70–7.75 (3H, m, H_{Ar}), 7.45–7.60 (12H, m, H_{Ar}), 7.02–7.05 (2H, dd, J = 10.5, 10.5, H_{Ar}), 5.83 (2H, s, C(1^1)H_2), 4.95–5.02 (2H, d, J = 20.0, C(2^1)H_2), 2.45 (9H, s, $H_{Ar}CH_3$); ^{13}C (500 MHz, DMSO-d_6, room temperature) δ_C 147.1, 138.7, 135.7, 134.8, 131.2, 123.8, 123.5, 115.6, 114.8 (Ar), 52.9, 21.8; HRMS (ESI): *m/z* calculated for $[M\text{-}HBr]^+$ $C_{37}H_{34}N_4O_2P$, 597.2419, found 597.2412.

2.1.28. (2-(1-(2-nitrobenzyl)-1H-1, 2, 3-triazol-4-yl) benzyl) tri-p-tolyl phosphonium bromide (2c)

Yield: (0.234 g, 70 %) as a white solid. mp 286–288 °C; IR: v_{max}/cm^{-1}: 3032 (sp^3 C—H) 1598, 1525, 864 (Ar C=C-H), 565–450 (ArP-C); ^{1}H NMR (500 MHz, DMSO-d_6, room temperature): δ_H 8.54 (1H, s, C(5) $H_{triazole}$), 8.12–8.15 (2H, d, J = 10.5, Ar —H), 7.40–7.60 (14H, m, ArH), 7.17–7.19 (1H, d, J = 8.0, Ar—H), 6.89–7.02 (2H, dd, J = 9.0, 8.5, Ar—H), 5.96 (2H, s, C(1^1)H_2), 5.05 (2H, d, J = 16.0, C(2^1)H_2); 2.42 (9H, s, $H_{Ar}CH_3$); ^{13}C (500 MHz, DMSO-d_6, room temperature) δ_C, 135.0, 134.5, 131.9, 134.5, 131.2, 130.4, 125.9, 123.4 (Ar), 50.8, 21.8; HRMS (ESI): *m/z* calculated for $[M\text{-}HBr]^+$ $C_{37}H_{34}N_4O_2P$, 597.2366, found 597.2366.

2.1.29. (2-(1-(4-chlorobenzyl)-1H-1,2,3-triazol-4-yl)benzyl)tri-p-tolylphosphonium bromide (2d)

Yield: (0.234 g, 70 %) as a white solid. mp 266–268 °C; IR: v_{max}/cm^{-1}: 3014 (sp^3 C—H) 1597, 1476, 857 (Ar C=C-H), 565–450 (Ar-P-C); ^{1}H NMR (500 MHz, DMSO-d_6, room temperature): δ_H 8.59 (1H, s, C(5) $H_{triazole}$), 7.67–7.70 (2H, d, J = 7.50, H_{Ar}), 7.42–7.54 (12H, m, H_{Ar}), 7.37–7.41 (3H, m, H_{Ar}), 7.27 (1H, m, H_{Ar}), 6.97–7.01 (2H, dd, J = 10.0, 10.0, H_{Ar}), 5.63 (2H, s, C(1^1)H^2), 5.02 (2H, d, J = 16.0, C(2^1)H_2); 2.41 (9H, s, $H_{Ar}CH_3$); ^{13}C (500 MHz, DMSO-d_6, room temperature) δ_C 146.6, 138.8, 134.4, 131.2, 128.7, 127.2, 122.6, 115.5, 114.8 (Ar), 52.9, 21.7; HRMS (ESI): *m/z* calculated for $[M + H]^+$ $C_{37}H_{34}^{35}ClN_3P^+$, 586.2179 found 586.2184. Calculated for $[M\text{-}HBr]^+$ $C_{37}H_{34}^{37}ClN_3P$, 588.2179, found 587.2210.

2.1.30. (2-(1-(3-chlorobenzyl)-1H-1, 2,3-triazol-4-yl)benzyl)tri-p-tolyl-phosphonium bromide (2e)

Yield: (0.224 g, 68 %) as a white solid. mp 255–258 °C; IR: v_{max}/cm^{-1}: 3014 (sp^3 C—H) 1597, 1476, 857 (Ar C=C-H), 565–450 (Ar-P-C); ^{1}H NMR (500 MHz, DMSO-d_6, room temperature): δ_H 8.59 (1H, s, C(5) $H_{triazole}$), 7.67–7.70 (2H, d, J = 7.50, H_{Ar}), 7.42–7.54 (12H, m, H_{Ar}), 7.37–7.41 (3H, m, H_{Ar}), 7.27 (1H, m, H_{Ar}), 6.97–7.01 (2H, dd, J = 10.0, 10.0, H_{Ar}), 5.63 (2H, s, C(1^1)H^2), 5.02 (2H, d, J = 16.0, C(2^1)H_2); 2.41 (9H, s, $H_{Ar}CH_3$); ^{13}C (500 MHz, DMSO-d_6, room temperature) δ_C 146.6, 138.8, 134.4, 131.2, 128.7, 127.2, 122.6, 115.5, 114.8 (Ar), 52.9, 21.7; HRMS (ESI): *m/z* calculated for $[M + H]^+$ $C_{37}H_{34}^{35}ClN_3P^+$, 586.2179 found 586.2184. Calculated for $[M\text{-}HBr]^+$ $C_{37}H_{34}^{37}ClN_3P$, 588.2179, found 587.2210.

2.1.31. 2-(1-(2-chlorobenzyl)-1H-1,2,3-triazol-4-yl)benzyl)tri-p-tolylphosphonium bromide (2f)

Yield (0.234 g, 70 %) as a white solid. mp 280–283 °C; IR: v_{max}/cm^{-1}: 3014 (sp^3 C—H) 1597, 1476, 857 (Ar C=C-H), 565–450 (Ar-P-C); ^{1}H NMR (500 MHz, DMSO-d_6, room temperature): δ_H 8.59 (1H, s, C(5) $H_{triazole}$), 7.67–7.70 (2H, d, J = 7.50, H_{Ar}), 7.42–7.54 (12H, m, H_{Ar}), 7.37–7.41 (3H, m, H_{Ar}), 7.27 (1H, m, H_{Ar}), 6.97–7.01 (2H, dd, J = 10.0, 10.0, H_{Ar}), 5.63 (2H, s, C(1^1)H^2), 5.02 (2H, d, J = 16.0, C(2^1)H_2); 2.41 (9H, s, $H_{Ar}CH_3$); ^{13}C (500 MHz, DMSO-d_6, room temperature) δ_C 146.6, 138.8, 134.4, 131.2, 128.7, 127.2, 122.6, 115.5, 114.8 (Ar), 52.9, 21.7; HRMS (ESI): *m/z* calculated for $[M + H]^+$ $C_{37}H_{34}^{35}ClN_3P^+$, 586.2179 found 586.2184. Calculated for $[M\text{-}HBr]^+$ $C_{37}H_{34}^{37}ClN_3P$, 588.2179, found 587.2210.

2.1.32. 2-(1-benzyl-1H-1,2,3-triazol-4-yl)benzyl)tri-p-tolylphosphonium bromide (2 g)

Yield (0.138 g, 62 %) as a white solid. mp 282–284 °C; IR: v_{max}/cm^{-1}: 3014 (sp^3 C—H) 1597, 1476, 857 (Ar C=C-H), 565–450 (Ar-P-C); ^{1}H NMR (500 MHz, DMSO-d_6, room temperature): δ_H 7.63 (1H, s, C(5) $H_{triazole}$), 7.27–7.37 (2H, d, J = 7.50, H_{Ar}), 7.16–7.28 (12H, m, H_{Ar}), 7.27–7.58 (4H, m, H_{Ar}), 7.37 (5H, m, H_{Ar}), 5.48 (2H, s, C(1^1)H^2), 5.02 (2H, d, J = 16.0, C(2^1)H_2); 2.37 (9H, s, $H_{Ar}CH_3$); ^{13}C (500 MHz, DMSO-d_6, room temperature) δ_C 146.6, 138.8, 134.4, 131.2, 128.7, 127.2, 122.6, 115.5, 114.8 (Ar), 52.9, 21.7; HRMS (ESI): *m/z* calculated for $[M + H]^+$ $C_{37}H_{35}N_3P^+$, 552.2563; found 552.2560.

2.1.33. tris-(4-(fluorophenyl)(2–1-(4-nitrobenzyl)-1H-1,2,3-triazol-4-yl) benzyl phosphonium bromide (3a)

Yield: (0.223 g, 67 %) as a white solid; mp 256–259 °C; IR: v_{max}/cm^{-1}: 3000 (sp^3 C—H) 1591, 1501, 828 (Ar C=C-H), 565–450 (ArP-C); ^{1}H NMR (500 MHz, DMSO-d_6, room temperature): δ_H 8.17 (1H, s, C(5) $H_{triazole}$), 7.76–7.79 (2H, d, J = 8.5, H_{Ar}), 7.26–7.32 (8H, m, H_{Ar}), 7.14–7.20 (6H, m, H_{Ar}), 7.08 (2H, d, J = 10.5, H_{Ar}), 6.54–6.57 (2H, dd, J = 10.5, 10.5, H_{Ar}), 5.36 (2H, s, C(1^1)H_2), 5.15–5.21 (2H, d, J = 16.0, C (2^1)H_2); ^{13}C (500 MHz, DMSO-d_6, room temperature) δ_C 175.3, 171.8, 137.9, 131.9, 133.9, 128.4, 126.1, 125.4 (Ar), 52.1, 28.5; HRMS (ESI): *m/z* calculated for $[M\text{-}HBr]^+$ $C_{33}H_{23}F_3N_4O_2P$, 609.1659, found 609.1659.

2.1.34. tris-(4-(fluorophenyl)(2–1-(3-nitrobenzyl)-1H-1,2,3-triazol-4-yl) benzyl phosphonium bromide (3b).

(0.220 g, 67 %) as a white solid. mp 264–266 °C; IR: v_{max}/cm^{-1}: 2981 (sp^3 C—H) 1591, 1501, 828 (Ar C=C-H), 565–450 (ArP-C); ^{1}H NMR (500 MHz, DMSO-d_6, room temperature): δ_H 8.14 (1H, s, C(5) $H_{triazole}$), 7.70–7.74 (2H, m, ArH), 7.09–7.33 (16H, m, H_{Ar}), 6.62–6.68 (1H, m, H_{Ar}), 6.50–6.52 (2H, m, H_{Ar}), 5.32 (1H, s, C(1^1)H_2), 4.62–4.68 (2H, d, J = 20.0, C(2^1)H_2; ^{13}C (500 MHz, DMSO-d_6, room temperature) δ_C:138.0, 137.6, 134.1, 131.5, 130.6, 128.9, 126.1, 125.7, 123.2, 123.0, 122.3, 118.0, 117.9, 117.7 (Ar), 79.5, 52.3, 28.5; HRMS (ESI): *m/z* calculated for $[M\text{-}HBr]^+$ $C_{33}H_{23}F_3N_4O_2P$, 609.1667, found 609.1669.

2.1.35. tris-(4-(fluorophenyl) (4–1-(2-nitrobenzyl)-1H-1, 2, 3-triazol-4-yl) benzyl phosphonium bromide (3c)

Yield (0.200 g, 60 %) as a white solid; mp: 271–274 °C; IR: v_{max}/cm^{-1}: 3000 (sp^3 C—H) 1591, 1501, 828 (Ar C=C-H), 565–450 (ArP-C);

^{1}H NMR (500 MHz, DMSO-d_6, room temperature): δ_H 8.55 (1H, s, C(5)$H_{triazole}$), 7.70–7.78 (10H, m, H_{Ar}), 7.58–7.66 (7H, m, H_{Ar}), 7.18 (1H, m, H_{Ar}), 6.98–7.04 (2H, dd, J = 8.5, 8.0, H_{Ar}), 5.96 (2H, s, C(1^1)H_2), 5.13–5.19 (2H, d, J = 16.0, C(2^1)H_2); ^{13}C (500 MHz, DMSO-d_6, room temperature) δ_C:167.8, 165.8, 148.1, 146.0, 138.1, 134.8, 131.1, 130.2, 125.7, 118.5, 114.7 (Ar), 50.8, 22.9; HRMS (ESI): *m/z* calculated for [M-HBr]$^+$ $C_{33}H_{23}F_3N_4O_2P$, 609.1665, found 609.1665.

2.1.36. tris-(4-(fluorophenyl)(2–1-(4-chlorobenzyl)-1H-1, 2, 3-triazol-4-yl)benzyl phosphonium bromide (3d).

Yield: (0.1708 g, 60 %) as a white solid; mp 242–245 °C; IR:v_{max}/cm^{-1}: 3017 (sp^3 C—H) 1589, 1500, 858 (Ar C=C-H), 565–450 (Ar-P-C); ^{1}H NMR (500 MHz, DMSO-d_6, room temperature) δ_H 8.64 (1H, s, C(5)$H_{triazole}$), 7.75–7.85 (10H, m, H_{Ar}), 7.60–7.70 (7H, m, ArH), 7.40–7.45 (3H, m, H_{Ar}), 7.00–7.05 (2H, m, H_{Ar}), 5.67 (2H, s, C(1^1)H_2), 5.15–5.21 (2H, d, J = 20.0, C(2^1)H_2); ^{13}C (500 MHz, DMSO-d_6, room temperature) δ_C 167.7, 166.0, 146.3, 138.7, 138.0, 132.0, 130.7, 122.9, 118.5, 114.6 (Ar), 52.9, 29.2; HRMS (ESI): *m/z* calculated for [M-HBr]$^+$ $C_{34}H^{35}_{24}ClF_3N_3P$, 598.1427, found 598.1427. Calculated for [M-HBr]$^+$ $C_{34}H^{37}_{24}ClF_3N_3P$, 600.1247, found 600.1414.

2.1.37. tris-(4-(fluorophenyl)(2–1-(3-chlorobenzyl)-1H-1, 2, 3-triazol-4-yl)benzyl phosphonium bromide (3e)

Yield: (0.1509 g, 53 %) as a white solid; mp 247–249 °C; IR:v_{max}/cm^{-1}: 3017 (sp^3 C—H) 1589, 1500, 858 (Ar C=C-H), 565–450 (Ar-P-C); ^{1}H NMR (500 MHz, DMSO-d_6, room temperature) δ_H 8.64 (1H, s, C(5)$H_{triazole}$), 7.75–7.85 (10H, m, H_{Ar}), 7.60–7.70 (7H, m, ArH), 7.40–7.45 (3H, m, H_{Ar}), 7.00–7.05 (2H, m, H_{Ar}), 5.67 (2H, s, C(1^1)H_2), 5.15–5.21 (2H, d, J = 20.0, C(2^1)H_2); ^{13}C (500 MHz, DMSO-d_6, room temperature) δ_C 167.7, 166.0, 146.3, 138.7, 138.0, 132.0, 130.7, 122.9, 118.5, 114.6 (Ar), 52.9, 29.2; HRMS (ESI): *m/z* calculated for [M-HBr]$^+$ $C_{34}H^{35}_{24}ClF_3N_3P$, 598.1427, found 598.1427. Calculated for [M-HBr]$^+$ $C_{34}H^{37}_{24}ClF_3N_3P$, 600.1247, found 600.1414.

2.1.38. tris-(4-(fluorophenyl)(2–1-(2-chlorobenzyl)-1H-1, 2, 3-triazol-4-yl)benzyl phosphonium bromide (3f)

Yield: (0.1620 g, 57 %) as a white solid; mp 237–239 °C; IR:v_{max}/cm^{-1}: 3017 (sp^3 C—H) 1589, 1500, 858 (Ar C=C-H), 565–450 (Ar-P-C); ^{1}H NMR (500 MHz, DMSO-d_6, room temperature) δ_H 8.64 (1H, s, C(5)$H_{triazole}$), 7.75–7.85 (10H, m, H_{Ar}), 7.60–7.70 (7H, m, ArH), 7.40–7.45 (3H, m, H_{Ar}), 7.00–7.05 (2H, m, H_{Ar}), 5.67 (2H, s, C(1^1)H_2), 5.15–5.21 (2H, d, J = 20.0, C(2^1)H_2); δ_P 22.3; ^{13}C (500 MHz, DMSO-d_6, room temperature) δ_C 167.7, 166.0, 146.3, 138.7, 138.0, 132.0, 130.7, 122.9, 118.5, 114.6 (Ar), 52.9, 29.2; HRMS (ESI): *m/z* calculated for [M-HBr]$^+$ $C_{34}H^{35}_{24}ClF_3N_3P$, 598.1427, found 598.1427. Calculated for [M-HBr]$^+$ $C_{34}H^{37}_{24}ClF_3N_3P$, 600.1247, found 600.1414.

2.1.39. 2-(1-benzyl-1H-1,2, 3-triazol-4-yl)benzyl)tris(4-fluorophenyl) phosphonium

Yield: (0.1847 g, 65 %) as a white solid. mp: 271–274 °C; IR: v_{max}/cm^{-1}: 3000 (sp^3 C—H) 1591, 1501, 828 (Ar C=C-H), 565–450 (ArP-C); ^{1}H NMR (500 MHz, DMSO-d_6, room temperature): δ_H 8.55 (1H, s, C(5)$H_{triazole}$), 7.37 (3H, m, H_{Ar}), 7.58 (2H, m, H_{Ar}), 7.20 (6H, m, H_{Ar}), 7.31 (6H, m, H_{Ar}), 7.27 (4H, m, H_{Ar}), 5.96 (2H, s, C(1^1)H_2), 5.48 (2H, d, J = 16.0, C(2^1)H_2);; ^{13}C (500 MHz, DMSO-d_6, room temperature) δ_C:167.8, 165.8, 148.1, 146.0, 138.1, 134.8, 131.1, 130.2, 125.7, 118.5, 114.7 (Ar), 50.8, 22.9; HRMS (ESI): *m/z* calculated for [M-HBr]$^+$ $C_{34}H_{26}F_3N_3P$, 564.1810, found 564.1820.

2.1.40. Antitubercular screening

The protocol for the antitubercular evaluation was developed at the Noguchi Memorial Institute for Medical Research, which was adapted from [31].

2.1.41. Antitubercular assays

2.1.41.1. Preparation of standard solutions of selected phosphonium salts. The 21 phosphonium salt compounds were selected for preliminary testing. 10 mg of each of the compounds was accurately weighed and dissolved in dimethyl sulfoxide (DMSO) (10 mL) to obtain a concentration of 1 mg/mL. The solution was further diluted with 10 mL of DMSO to obtain a concentration of 100 µg/mL. A 2-fold dilution of the stock concentration was pipetted into an Eppendorf tube, vortexed for 45 s, and spun for 5 min to obtain a new concentration of 50 µg/mL. 500 µL was then pipetted into a second tube containing 500 µL of the diluent to obtain a new concentration of 25 µg/mL. The final solution (25 µg/mL) was diluted serially to obtain the following: 12.5, 6.25, 3.125, and 1.5625 µg/mL. Isoniazid (0.1 µg/mL) and rifampicin (1.0 µg/mL) were used as reference drugs and dissolved in sterile water to obtain their respective final concentrations according to the manufacturer's instructions for positive control.

2.1.42. Detection of Mycobacterium tuberculosis by BACTEC MGIT 960 method

The BACTEC 960 assay, using liquid culture, detected the antitubercular activity of active compounds against *M. tuberculosis*. The BACTEC MGIT 960 system basically uses a Middlebrook 7H9 base enriched with additional supplements (OADC). *Mycobacterium tuberculosis* utilizes oxygen flashed in the MGIT, which is acting as a quencher to the fluorescent molecule embedded in the BACTEC 960 to detect either susceptibility or resistance [32].

2.1.42.1. General protocol for BACTEC 960 fluorescence detection assay. Following the manufacturer's instructions, *Mycobacterium tuberculosis* (H37Rv) was cultured until detected positive by the Mycobacterium Growth Indicator Tube (MGIT) 960 using the Middle brook 7H9 media (Becton, Dickson and Company, USA). The test compounds were suspended in their suitable solvent to obtain 100 µg /mL. 800 µL of oleic acid-albumin-dextrose (OADC) was pipetted and mixed with PANTA (polymyxin B, amphotericin B, nalidixic acid, and azlocillin), which was previously reconstituted and stored at 2–8 °C, into the MGIT. 100 µL of the suspended synthetic compound (see sub-section 3.4.2.1) was pipetted and transferred aseptically into the MGIT. A tube without drugs was used as the negative control. After standardizing the inoculum (H_{37}Rv) with 0.5 McFarland solution, 500 µL of the inoculum was pipetted and transferred into the MGIT. The final mixture was transferred into the appropriate station of the BACTEC MGIT 960. The BACTEC MGIT 960 interpreted the results as either sensitive or resistant.

2.1.42.2. In- vitro cytotoxicity determination for murine macrophage cell line: MTT assay. The 50 % inhibitory concentration (IC_{50}) of the five selected most active phosphonium salts against H3R7V and 50 % cytotoxic concentration (CC_{50}) on murine macrophage cell line were obtained from dose response curve fit to the data by means of GraphPad Prism 6 software. The evaluations were performed in triplicate. The selectivity index (SI) was calculated using:

$$SI = \frac{50\%\text{inhibitory concentration on bacilli}}{50\%\text{cytotoxic concentration on macrophages}}$$

The antitubercular and cytotoxic activities are represented and summarised in Table 3 and Fig. 4.

2.1.42.3. Computational design. **A total of seventeen protein targets from *Mycobacterium tuberculosis* were selected for molecular docking to investigate the potential antitubercular mechanisms of phosphonium salts.** These targets include Pantothenic Kinase (PDB ID: 4BFT), Polyketide synthase 13 thioesterase domain (PDB ID: 5V3X), Serine/Threonine-Protein Kinase PknB Catalytic Domain (PDB ID: 2FUM), L,D-Transpeptidase 2 (PDB ID: 8J65), Enoyl-CoA Hydratase

EchA6 (PDB ID: 5DUF), Caseinolytic Peptidase C2 (PDB ID: 8ADA), Decaprenylphosphoryl-β-D-ribose-2′-epimerase (PDB IDs: 4P8N), Alkyl Hydroperoxide Reductase (PDB ID: 1KNC), Putative Lipoprotein Lppa (PDB ID: 2V7S), Caseinolytic Peptidase C1 (PDB ID: 8B9U), DNA Gyrase (PDB ID: 3M4I), ATP-binding Enzyme Rv3168 (PDB ID: 3ATT), Leucyl-tRNA Synthetase (PDB ID: 7PQK), Isocitrate Lyase (PDB ID: 6XPP), Glutamine-binding Solute-binding Proglutamine-binding lipoprotein GlnH (PDB ID: 6H2T), β-ketoacyl ACP synthase I (PDB ID: 2WGE), and Enoyl-Acyl Carrier Protein Reductase (PDB ID: 5MTP). These enzymes are crucial for the survival and disease-causing ability of *M. tuberculosis*, as they are involved in important processes like DNA copying, making folic acid, breaking down fats, building proteins, and forming the cell wall [33]. Therefore, inhibition of any of these proteins may impair the survival of *Mycobacterium tuberculosis* by disrupting nucleic acid cleavage, assembly, and replication processes; interfering with protein synthesis and transport of essential biomolecules; or by compromising the structure and functions of the bacterial cell walls [34]. To prepare the protein structure for docking, Discovery Studio Visualizer and UCSF Chimera software were employed. These tools facilitated the deletion of heteroatoms and duplicate chains, repair of truncated side chains, addition of hydrogen atoms, and assignment of partial charges [35]. The protein was saved in PDB format for easy recognition by Autodock tools [36,37]. The ligands were processed using LigPrep, available in Maestro, to build low-energy three dimensional structures with acceptable ionization states at physiological pH [38]. Molecular docking was performed using Autodock Vina [39], and the findings were evaluated using Discovery Studio 2021 software [40]. The methodology was validated *via* a molecular re-docking approach [41]. The total binding free energy (ΔG) was calculated using the Prime MM/GBSA module [42], providing an estimate of the stability of the protein–ligand complexes. Also, the ADME-Tox (Absorption, Distribution, Metabolism, Excretion, and Toxicity) properties of the compounds were estimated using the SWISSADME and ADMETlab 3.0 web servers. GROMACS 2023.3 software was used to study ligand-induced conformational changes and the dynamic behavior of protein-ligand complexes across time. The protein topology was generated using the CHARMM36 force field in GROMACS, while topology and parameter files for INH and the hit compounds were derived using the CGenFF-based ParamChem server and converted to GROMACS format. The protein-ligand complexes were surrounded by a simple water model in a cube shape, with water molecules placed 10 Å apart. The complex systems' total charge was neutralized by balancing the required counter ions of sodium and chloride with the physiological salt concentration of 0.15 M. The solvated systems were relaxed by energy minimization using steepest descent with a maximum of 5000 steps. Following that, the prepared systems were equilibrated under NPT and NVT ensemble conditions (constant number of atoms, volume, pressure, and temperature) for 1000 ps at 300 K and 1 bar, respectively. The Particle-Mesh Ewald (PME) approach was used to address van der Waals and long-range electrostatic interactions. Simulations were produced in 100 ns for each system, with coordinate trajectories stored every 10 ps. The results were analyzed using the built-in tools included with the GROMACS package. The g_rmsd, g_rmsf, g_gyrate, and g_sasa utilities were used to assess structural stability indices including RMSD, RMSF, Rg, and SASA.

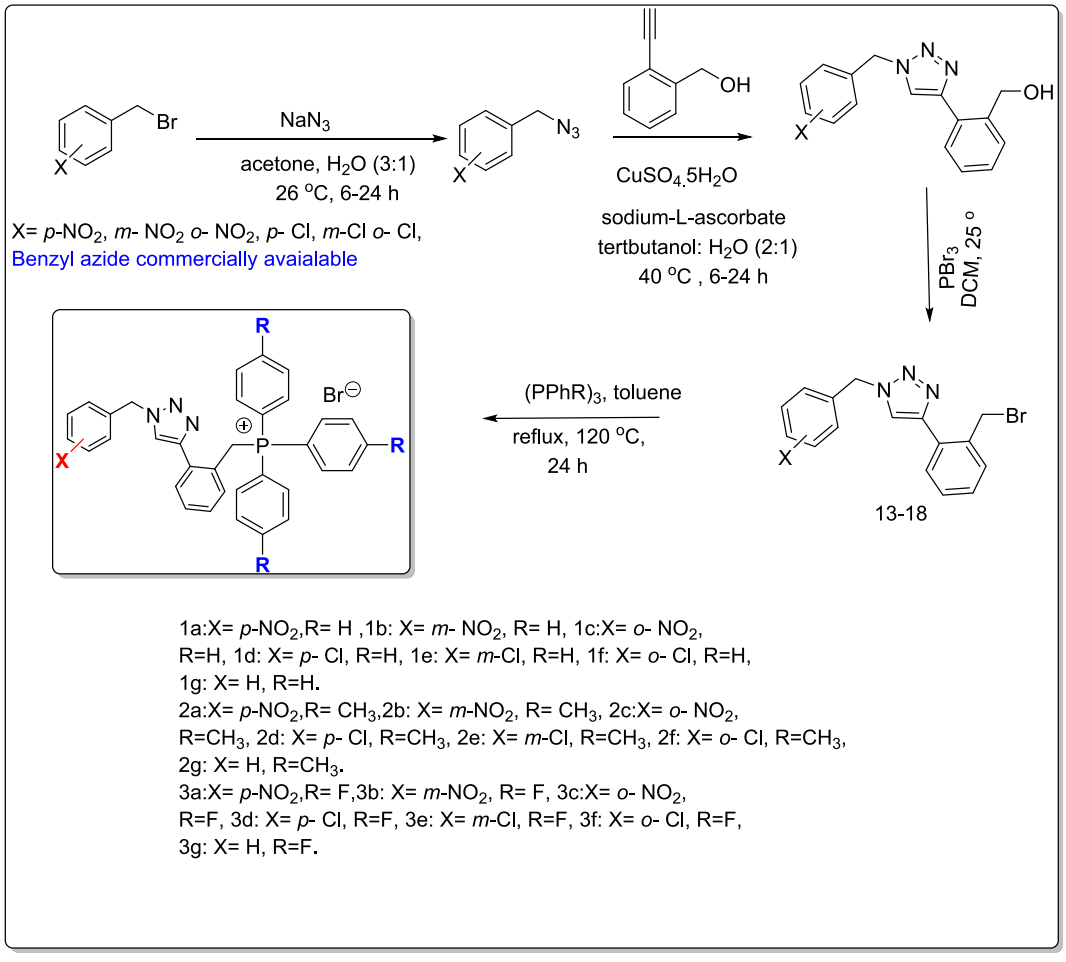

Fig. 3. A four-step synthetic procedure for the phosphonium salts.

3. Results and discussion

3.1. Chemistry

The 1,4-disubstituted 1,2,3-triazoles have been synthesized by the reaction of substituted benzyl azides and 2-ethynyl benzyl alcohol *via* click chemistry (Fig. 3). The benzyl azides have been afforded from corresponding benzyl bromides, according to Kekessie and co-workers 2022. The CuAAC reaction was performed in tert-butanol: water (2:1) at room temperature for 6–12 h to afford the 1,4-disubstituted 1,2,3-triazoles. The structures of the compounds were elucidated by ^{1}H NMR, ^{13}C NMR and HRMS spectroscopy. From the ^{1}H NMR spectrum of compound **2e**, which was the most potent compound against 17 targeted MTB proteins, the two methylene groups presented with singlet and doublet signals at 5.20 and 5.67 ppm, respectively. The singlet peak resonating downfield at 7.64 ppm represents the triazole proton. The presence of the methylene carbon attached to the nitrogen of the triazole calculated mass for $[M + Na]^{+}$ is 333.0958, and the observed peak in HRMS is 333.0958. From the structure elucidation, the compound **2e** was named as (2-(1-(3-chlorobenzyl)-1H-1, 2, 3-triazol-4-yl) benzyl) tri-*p*-tolylphosphonium bromide **(2e).** The 1, 4-disubstituted 1, 2, 3-triazole derivatives were synthetically transformed to afford three series: 1a-1 g, 2a-2 g, and 3a-3 g with electron-withdrawing groups on the aromatic core and various substituents on the phosphonium warhead have been synthesized in good to excellent yields (53–85 %). The series **(3a-3 g)** bearing the fluoro substituent on the aromatic ring on the left flank of the triazole generally gave the lowest yield of 53–67 %, with **(1a-1 g)** and **(2a-2 g)** showing the highest yields of 68–85 % and 68–80 %, respectively.

Clearly, the presence of the substitution or otherwise on the phosphonium head was a major determinant of the % yields, as unsubstituted or methyl-substituted phosphonium heads afforded a higher yield compared to their electron-withdrawing fluoro-substituted phosphonium heads. All the yields were above 60 % for the substituted triazoles, with the *meta* and *para* chloro and nitro derivatives showing the relatively highest yields above 75 %. The shorter reaction times relative to the unsubstituted aromatic azides and triazoles showed that the nitro- and chloro-substituted azides improved the kinetics of the copper-catalyzed azide-alkyne cycloaddition (CuACC) 'click' reaction. Moreover, the presence of a p- or *m*-nitro group increased the kinetics of the reaction; hence, the time for formation of the 1, 2, 3-triazoles was 6–12 h compared to 16–24 h for the other derivatives. For instance, the formation of the azide from the benzyl bromides is an SN_2 reaction which is dependent on the nature of the leaving group and the type of alkyl halide. Since all the benzyl bromides used were primary alkyl halides, the nature of the leaving group became a major contributing factor for the kinetics. The presence of an electron withdrawing groups such as chlorine and NO_2 regardless of their vector positions increase the rate at which bromine has to be substituted by the nucleophile azide. The unsubstituted benzyl bromides had a slow rate of reaction due to the absence of any of these electron withdrawing groups. The triazoles were further transformed using tribromophosphine to produce six (6) brominated compounds (**compounds 13–18**). The *p*-brominated compound had the highest yield of 96 %, due to reduced steric hindrance compared to their *ortho* and *meta* counterparts while the unsubstituted benzyl having the lowest yield of 60 %. The formation of the brominated intermediate compounds was key in the reaction pathway to allow easy synthetic transformation of the benzyl bromine to their respective phosphonium salts. The brominated compounds (13–18) were reacted with various phosphines to obtain their respective phosphonium salts, with twenty-one (21) of them synthesized in three series **(1a-1 g, 2a-3 g, 3a-3 g)** [Table 1]. The clicked and brominated compounds were purified by silica column chromatography in a gradient elution manner using Petroleum ether: ethyl acetate starting with 100 % *v*/v Petroleum ether to 60 % v/v Ethyl acetate: 40 % v/v Petroleum ether to afford white to beige solid products. The phosphonium salts which was purified by washing with toluene during suction filtration, all had yields above 70 % *w*/w. The purity of the compounds was confirmed by HPLC-HRMS and NMR, and they were determined to be isotopically pure (see supporting information for chromatograms, mass, and NMR spectra.

Table 1
Phosphonium salts' activity and growth inhibitory trend against MTB H37R$_V$.

Series	Compound	X	R	Growth Colony forming units				% inhibition at MIC
				1.56 (μg/ml)	6.25(μg/ml)	25(μg/ml)	100(μg/ml)	
1	1a	*p*-NO_2	H	400	400	168	168	58
	1b	*m*-NO_2	H	400	400	400	400	0
	1c	*o*-NO_2	H	400	400	400	400	0
	1d	*p*-cl	H	400	0	0	2	99.5
	1e	*m*-cl	H	400	0	0	0	100
	1f	*o*-cl	H	400	400	400	2	99.5
	1 g	H	H	400	400	400	0	100
2	2a	*p*-NO_2	CH_3	400	400	168	168	58
	2b	*m*-NO_2	CH_3	400	400	400	400	0
	2c	*o*-NO_2	CH_3	400	400	400	400	0
	2d	*p*-cl	CH_3	400	400	168	168	58
	2e	*m*-cl	CH_3	400	400	0	0	100
	2f	*o*-cl	CH_3	400	400	400	400	0
	2 g	H	CH_3	400	400	400	400	0
	3a	*p*-NO_2	F	400	400	400	0	100
3	3b	*m*-NO_2	F	400	400	400	400	0
	3c	*o*-NO_2	F	400	400	400	400	0
	3d	*p*-cl	F	400	400	168	168	58
	3e	*m*-cl	F	400	400	0	168	58
	3f	*o*-cl	F	400	400	0	168	58
	3 g	H	F	400	400	168	168	58
INH	Isoniazid	–	–	0	0	0	0	0
RMP	Rifampicin	–	–	0	0	0	0	0
PRN	Pyrazinamide	–	–	0	0	0	0	0
ETB	Ethambutol	–	–	0	0	0	0	0

GC: Growth Control (negative control); GCU: Growth Colony Unit; **1a-1 g, 2a-2 g, 3a-3 g**, and **4a-4 g** were adapted as codes for the selected compounds. *nd: not determined.
NB* Standard drugs: Equivalent concentrations used: 100, 25, 6.25, and 1.56 μg/mL.

3.2. Biological evaluation

3.2.1. Anti-tubercular activity and cytotoxicity

Twenty-one (21) synthesized click-tethered phosphonium salts were evaluated for their *in vitro* antitubercular activity by measuring the inhibition of growth of *Mycobacterium tuberculosis* H37Rv (ATCC 27294) in liquid broth medium (Table 1). Nitroaromatics were selected as starting scaffolds due to their established role in antitubercular drug discovery, attributed to the release of nitroso free radicals *via* redox pathways, a mechanism that underlies their antimicrobial and antiparasitic effects [43,44]. Although nitro groups are often associated with toxicity concerns, their inclusion in drug development remains relevant and active [45]. The phosphonium moiety was incorporated for its high lipophilicity, which facilitates penetration of the thick mycobacterial cell envelope. Furthermore, the methyl and fluorine substituents on the phosphonium head serve as classical bioisosteres that can enhance lipophilicity, thus improving bacterial membrane permeability and intracellular accumulation. To merge these functional groups, 1,2,3-triazole recognized as a versatile pharmacophore was employed as a molecular bridge linking the nitroaromatic moiety to the phosphonium head. Triazoles have also been recognized as linkers to various pharmacophores such as thiazolylcarboxylate [46], quinazolinone [47] and isonicotinohydrazides [48]. Building on this design using a nitroaromatic pharmacophore, the synthesized nitroaromatic "click"-tethered phosphonium salts were subjected to biological screening against both *M. tuberculosis* H37Rv and multidrug-resistant TB (MDR-TB) strains. In a preliminary screening, the anti-mycobacterial activity of the synthesized compounds was evaluated at concentrations of 100, 25, 6.25, and 1.56 μg/mL using the BACTEC 960 fluorescence method. This screening protocol was validated with first-line anti-tubercular drugs, rifampicin as reference standards at equivalent concentrations of 100, 25, 6.25, and 1.56 μg/mL. Among the compounds, phosphonium derivatives **1d** and **1e** showed potent activity against *Mycobacterium tuberculosis* H37Rv (ATCC 27294), exhibiting 100 % inhibition at a MIC of 6.25 μg/mL. At a concentration of 100 μg/mL, compounds **1d** and **1e** inhibited multidrug-resistant TB (MDR-TB) colony-forming unit (CFU) growth by 96 % and 64 %, respectively, indicating notable anti-mycobacterial potential. Compounds **2e**, **3e**, and **3f** also showed inhibitory activity against H37Rv, with **2e** being the only one to display moderate efficacy (68 % inhibition) against MDR-TB at 100 μg/mL. In contrast, **3e** and **3f** were inactive against MDR-TB at the same concentration. Structure-activity relationship (SAR) analysis revealed that chloro-substituted derivatives exhibited enhanced anti-tubercular activity, with halogenated benzyl analogs consistently achieving 99–100 % CFU inhibition at concentrations between 6.25 and 25 μg/mL. Conversely, their non-halogenated counterparts showed significantly lower activity. The unique lipid-rich, multi-layered cell wall of *Mycobacterium tuberculosis*, which is largely impermeable due to the presence of mycolic acids, contributes to drug resistance. The high lipophilicity of the phosphonium salts likely enhances membrane permeability, facilitating delivery of the pharmacophoric 'clicked' aromatic or heterocyclic moieties into the bacterial cell. Further SAR insights indicate that antitubercular potency was significantly influenced by the nature of the substituents on the benzyl ring and phosphonium head [49]. Derivatives in the **3a–3 g** series exhibited lower activity compared to the standard drugs. Notably, replacing hydrogen atoms on the phosphonium head with electron-withdrawing fluorine atoms reduced inhibition of active bacilli to 58 %. Similarly, incorporation of electron-donating methyl groups into halogenated derivatives diminished their activity, underscoring the importance of electronic effects on biological activity.

With regards to the *in-vitro* cytotoxicity on the murine macrophage cell line, compound **2e** was the most selective for the *Mycobacterium* bacilli with a selectivity index (SI) of 1.08 (Table 3, Fig. 4) though there could be more room for improvement to increase the SI. Compound 3f, though one of the most active had high toxicity towards both the bacilli and murine macrophage cell line. Structure optimisation would be carried out on these five (5) potent compounds to improve their potency and selectivity against the bacilli instead of host mammalian cells.

The antitubercular activity of compound **2e** was comparable to that of Isoniazid at 100 μg/mL (Table 2). Interestingly, the MDR-TB strain, which demonstrated resistance to at least isoniazid and rifampicin, also showed resistance to streptomycin and pyrazinamide but remained susceptible to ethambutol, highlighting the limited effectiveness of current treatment options. Although electron-withdrawing groups such as nitro and chloro play a vital role in conferring anti-tubercular activity, lipophilicity emerged as a critical parameter in this study. Strong electron-withdrawing groups induce electron-deficient regions within the molecule, facilitating interactions with nucleophilic residues at receptor sites. Additionally, nitro groups may enhance bioactivity by

Table 2
Phosphonium salts' activity and growth inhibitory trend against MDR-TB.

Compound	Growth (Colony forming units) at given concentrations				% inhibition at MIC
	1.56 μg/mL	6.25 μg/mL	25 μg/mL	100 μg/mL	
1d	400	400	384	0	96
1e	400	400	255	0	64
2e	400	400	273	0	68
3e	400	400	400	400	0
3f	400	400	400	400	0
INH	0	0	0	0	0*
RMP	0	0	0	0	0*

GC: *Growth Control (negative control)*; GCU: *Growth colony Unit.* *nd: not determined.
NB*: Equivalent concentrations for each standard drug used: 100, 25, 6.25, and 1.56 μg/mL.

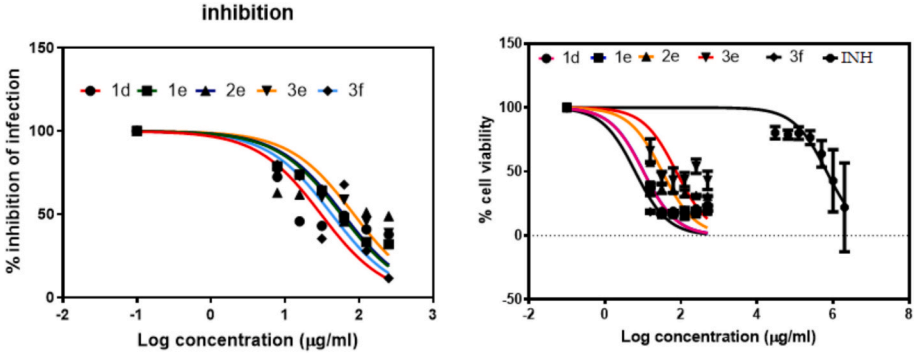

Fig. 4. [a] (left) Dose response curve for treatment of infected human murine macrophage cells [b] (right) dose response curve for cytotoxicity determination. [**1d**, **1e, 2e, 3e** and **3f**]: phosphonium salt test compounds, Isoniazid (standard antitubercular agent).

releasing nitrous free radicals that possess biological activity [50]. The enhanced lipophilicity observed in compound **2e**, as evidenced by its high LogP value of 3.09, which suggests increased partitioning into the lipid-rich mycobacterial membrane. This promotes localization at the receptor site and potentially prolongs the compound's duration of action. Moreover, the inclusion of chlorine atoms in drug structures is known to enhance *in vivo* metabolic stability. In conclusion, all the synthesized click-tethered phosphonium salts demonstrated promising activity against the *M. tuberculosis* H37Rv bacteria and are therefore potential candidates for further TB drug development. Compound **2e** had the highest selective index of 1.08 (Table 3) demonstrating least cytotoxicity towards the human murine macrophage cells though it requires optimisation to improve the cytotoxicity profile. Notably, **compounds 1d, 1e, and 2e** emerged as the most potent and promising scaffolds against multidrug-resistant TB (MDR-TB), a persistent global health threat.

3.3. Computational design

3.3.1. Pharmacokinetic and toxicity profile

The drug-likeness and ADMET (Absorption, Distribution, Metabolism, Excretion, Toxicity) properties of the synthesized compounds were evaluated *in silico* using the SwissADME and ADMETlab 3.0 platforms. The analysis focused on key physicochemical and pharmacokinetic parameters critical for oral bioavailability (Table 4).

All phosphonium salts conformed to established guidelines for drug-like molecules. Their molecular weights (MW) and calculated octanol-water partition coefficients (cLogP) were within acceptable ranges, suggesting a favorable balance between solubility and membrane permeability [51,52]. A notable feature was the absence of hydrogen-bond donors (HBD) across the series, which typically enhances passive diffusion across biological membranes. The number of hydrogen-bond acceptors (HBA) varied from 2 to 7, influencing aqueous solubility and potential target interactions [53]. Lipophilicity, a crucial factor for penetrating the lipid-rich mycobacterial cell wall, was highest for the chloro-substituted derivatives. For instance, the cLogP values for **1d** (5.43) and **2e** (6.41) indicate significant hydrophobic character, which likely contributes to their potent antitubercular activity by promoting accumulation within the bacilli [54].

Topological Polar Surface Area (TPSA), a strong predictor of cell permeability and oral absorption, was calculated for each compound. Derivatives with nitro substituents (**1a-c**, **2a-c**, **3a-c**) exhibited higher TPSA values (≈90 $Å^2$), correlating with moderately high predicted human intestinal absorption (77–78 %). In contrast, the chloro-substituted and unsubstituted analogs (**1d-g**, **2d-g**, **3d-g**) displayed lower TPSA values (44.3 $Å^2$), resulting in excellent predicted absorption rates of 93–94 %. This suggests that the latter group possesses superior membrane permeability [55–57].

The BOILED-Egg model (Brain Or IntestinaL EstimateD permeation) (Fig. 5Fig. 5) was employed to predict passive gastrointestinal absorption and blood-brain barrier (BBB) penetration. The model positioned the most active compounds (**1d**, **1e**, **2e**) within the region denoting high probability of intestinal absorption. Notably, these compounds were also predicted to cross the BBB, indicating potential efficacy against central nervous system tuberculosis. However, they were simultaneously identified as substrates for the P-glycoprotein (P-gp) efflux pump. This dual prediction is pharmacokinetically advantageous: BBB penetration allows for CNS activity, while P-gp mediated efflux may mitigate the risk of neurotoxic accumulation by actively removing the compounds from the brain [58].

Metabolism predictions indicated that the compounds are likely substrates for key cytochrome P450 enzymes, including CYP3A4, CYP2C19, CYP1A2, and CYP2C9. This suggests they would undergo hepatic metabolism, influencing their clearance rates and potential drug-drug interactions [59].

Initial toxicity profiling revealed concerns regarding potential cytotoxicity, a known challenge for phosphonium salts due to their ability to disrupt mitochondrial membranes. Genotoxicity and cardiotoxicity risks were also flagged *in silico*. However, the experimental selectivity index (SI) determined for the most active compounds, particularly **2e** (SI = 1.08), demonstrates a measurable *in vitro* window between antimycobacterial activity and mammalian cell cytotoxicity. This provides a preliminary safety benchmark and a clear starting point for future structural optimization to mitigate toxicity, such as exploring bioisosteric replacements for the phosphonium moiety [60,61].

3.3.2. Molecular docking

Molecular docking was performed to investigate the potential binding modes and affinities of the synthesized phosphonium salts against a panel of seventeen *Mycobacterium tuberculosis* target proteins. The primary objective was to identify the most probable protein target and elucidate the key interactions responsible for the observed antitubercular activity [62]. The docking protocol was validated by re-docking the native co-crystallized ligand into the binding site of the InhA enzyme (PDB ID: 5MTP). The resulting pose showed excellent agreement with the original crystallographic conformation, yielding a root mean square deviation (RMSD) of 0.10 Å. An RMSD value below 2.0 Å is widely accepted as indicative of a reliable docking methodology. The strong overlap between the experimental and predicted poses (Fig. 6a), along with the conservation of critical interaction patterns (Fig. 6b, c), confirms the robustness and accuracy of the employed docking parameters for subsequent virtual screening.

A heat map visualization of the raw docking scores across all 17 targets provided an initial overview of binding preferences (Fig. 7a). To enable a fair comparison between different protein targets and mitigate scoring biases inherent to diverse binding pockets, the docking scores were standardized using z-score normalization (Fig. 7b). This analysis revealed a consistent and pronounced trend. All synthesized compounds exhibited their strongest predicted binding affinities for Enoyl-Acyl Carrier Protein Reductase (InhA, PDB: 5MTP). This target emerged as a clear hotspot for interaction with this chemical series.

Among the compounds, **1d** displayed the most favorable docking score against InhA at −13.7 ± 0.15 kcal/mol, followed closely by **1e** and **2e**. In contrast, the same compounds showed significantly weaker binding affinities (less negative scores) for other targets such as Caseinolytic Peptidase C2 (8ADA) and Alkyl Hydroperoxide Reductase (1KNC). This selective computational affinity towards InhA strongly suggests it as the primary mechanistic target for this class of compounds [63]. To understand the basis for the lower affinity towards non-primary targets, interaction analysis were conducted for compounds **1d**, **1e**, and **2e** with proteins 8ADA and 1KNC (Table 5). The analysis revealed sparse and less complementary interaction networks. For instance, at the 8ADA binding site, interactions were limited to peripheral residues like ASP29, VAL72, and SER69 for **1d**, and involved fewer hydrophobic contacts compared to the InhA complex. Similarly, interactions with 1KNC were

Table 3
Antitubercular activity (IC_{50}), cytotoxicity profile (CC_{50}) and selectivity index (SI) of the most active compounds against $H37R_V$.

Compounds	$IC_{50\pm SEM\ (\mu M)}$ [a]	$CC^{b}_{50\pm SEM\ (\mu M)}$	SI [c]
1d	54.98 ± 0.035	8.14 ± 0.060	0.15
1e	30.22 ± 0.091	10.62 ± 0.090	0.35
2e	76.20 ± 0.058	82.11 ± 0.112	1.08
3e	68.21 ± 0.096	30.04 ± 0.053	0.44
3f	38.84 ± 0.126	4.32 ± 0.111	0.11
[e] **Isoniazid**	0.7 ± 0.006	No inhibition	Nd

[a] IC_{50} = 50% inhibitory concentration on H37Rv [b] CC_{50} = 50 % cytotoxic concentration on murine macrophage RAW 264.7 [c] SI = Selective index (CC_{50}/IC_{50}); [d] % inhibition during preliminary screening; Isoniazid, positive control. [a] IC_{50} and [b] CC_{50} values represent triplicate determinations (three determinations from three different experiments). Nd: no visible and significant inhibition hence SI determination not available.

Table 4
Predicted Physicochemical and Pharmacokinetic Properties of the Synthesized Compounds and Isoniazid.

Compound	MW	RB	HBA	HBD	MR	TPSA	cLogP	GIA	BBB	Pgp substrate	%ABS
1a	635.49	9	4	0	178.01	90.12	4.32	High	No	Yes	77.91
1b	635.49	9	4	0	178.01	90.12	4.34	High	No	Yes	77.91
1c	635.49	9	4	0	178.01	90.12	4.29	High	No	Yes	77.91
1d	624.94	8	2	0	174.2	44.3	5.43	High	Yes	Yes	93.72
1e	624.94	8	2	0	174.2	44.3	5.39	High	Yes	Yes	93.72
1f	624.94	8	2	0	174.2	44.3	5.39	High	Yes	Yes	93.72
1 g	590.49	8	2	0	169.19	44.3	4.91	High	Yes	Yes	93.72
2a	677.57	9	4	0	192.91	90.12	5.13	High	No	Yes	77.91
2b	677.57	9	4	0	192.91	90.12	5.1	High	No	Yes	77.91
2c	677.57	9	4	0	192.91	90.12	5.11	High	No	Yes	77.91
2d	667.02	8	2	0	189.1	44.3	6.44	High	Yes	Yes	93.72
2e	667.02	8	2	0	189.1	44.3	6.41	High	Yes	Yes	93.72
2f	667.02	8	2	0	189.1	44.3	6.4	High	Yes	Yes	93.72
2 g	632.57	8	2	0	184.09	44.3	5.89	High	Yes	Yes	93.72
3a	689.46	9	7	0	177.89	90.12	5	High	No	Yes	77.91
3b	689.46	9	7	0	177.89	90.12	5.06	High	No	Yes	77.91
3c	689.46	9	7	0	177.89	90.12	5.06	High	No	Yes	77.91
3d	678.91	8	5	0	174.07	44.3	6.37	High	Yes	Yes	93.72
3e	678.91	8	5	0	174.07	44.3	6.33	High	Yes	Yes	93.72
3f	678.91	8	5	0	174.07	44.3	6.34	High	Yes	Yes	93.72
3 g	644.46	8	5	0	169.06	44.3	5.88	High	Yes	Yes	93.72
INH	137.14	2	3	2	35.13	68.01	−0.35	High	No	No	85.54

Abbreviations: MW = Molecular Weight; RB = Number of Rotatable Bonds; HBA = Hydrogen Bond Acceptors; HBD = Hydrogen Bond Donors; TPSA = Topological Polar Surface Area; cLogP = Calculated logarithm of Partition coefficient; GI = Gastrointestinal; BBB = Blood-Brain Barrier; P-gp = P-glycoprotein; %ABS = Predicted Percentage Absorption.

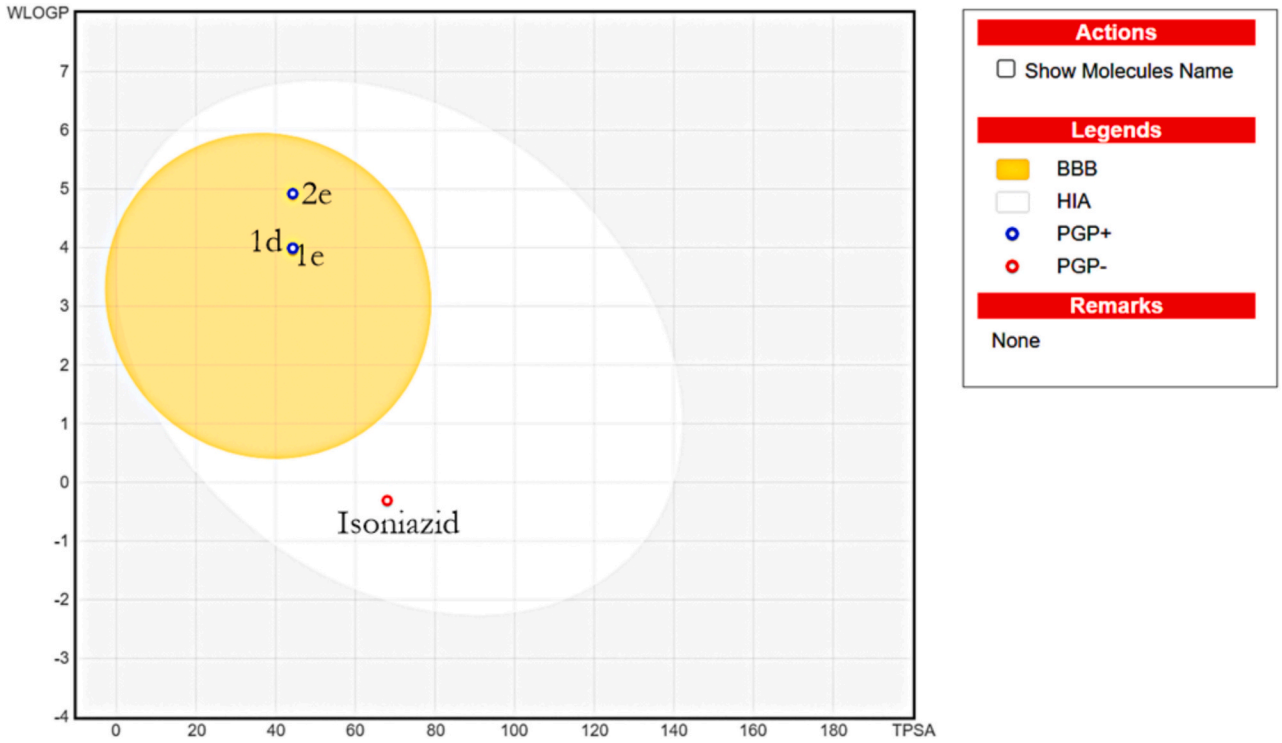

Fig. 5. BOILED-egg representation of the lead compounds.

less extensive and lacked engagement with core catalytic residues. Crucially, the central triazole ring and the benzyl chloride moiety failed to form equivalent stabilizing interactions with residues in these alternative targets, resulting in lower predicted stability and affinity In-depth analysis of the docking poses within the InhA (5MTP) active site revealed a complex network of interactions that explain the high binding scores. All three top compounds occupied the substrate-binding tunnel, engaging key catalytic and structural residues. The binding of **Compound 1d** is dominated by extensive hydrophobic interactions. The *para*-chlorobenzyl group inserts deeply into a hydrophobic subpocket, forming contacts with MET155, LEU218, PHE149, ALA157, PRO156, VAL203, and TYR158. The triazole ring engages MET199, while the phosphonium head group establishes additional van der Waals contacts. This creates a well-packed, energetically favorable complex. The *meta*-chlorobenzyl group of **Compound 1e** orients differently, forming hydrophobic contacts with LEU218, TYR158, ALA157, and VAL203, and a unique halogen (chlorine)-sulfur interaction with MET155. This variation in the chlorophenyl orientation alters the network slightly but maintains strong complementarity with the hydrophobic cleft. The binding mode of **Compound 2e** adapts to accommodate the methyl

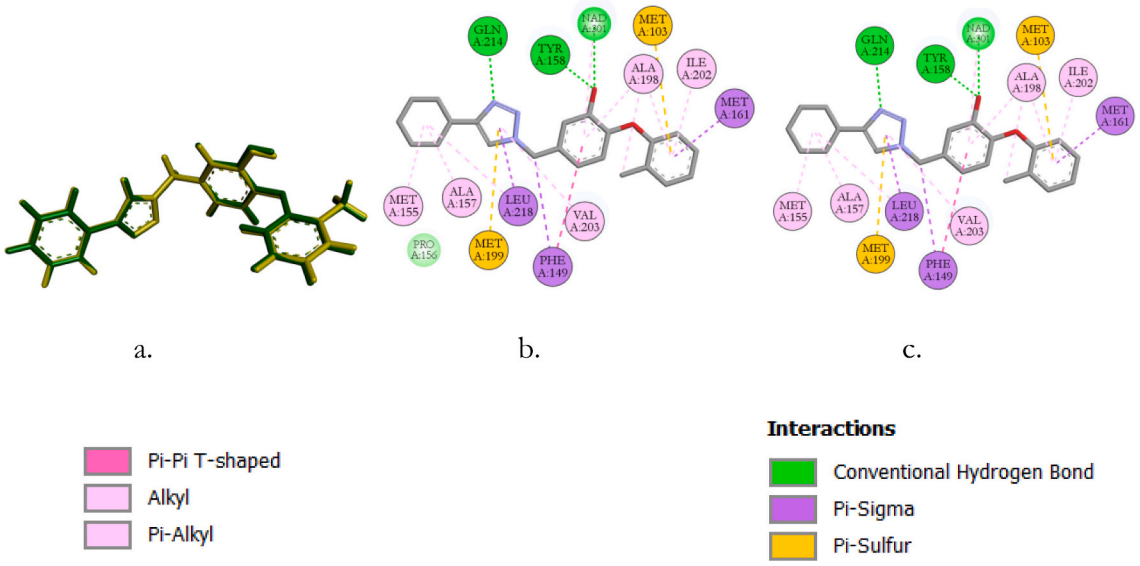

Fig. 6. Validation of docking protocol: Protein-ligand interaction analysis for the co-crystallized ligand (53 K) with the 5MTP protein structure is shown. Panel (a) represents the superimposition of the co-crystallized ligand (green) and the docked best pose (yellow), demonstrating strong overlap and confirming the reliability of the docking protocol. Panel (b) represents the binding pose of the ligand before the re-docking procedure (experimental/original pose), and panel (c) shows the pose after re-docking (predicted pose). (For interpretation of the references to colour in this figure legend, the reader is referred to the web version of this article.)

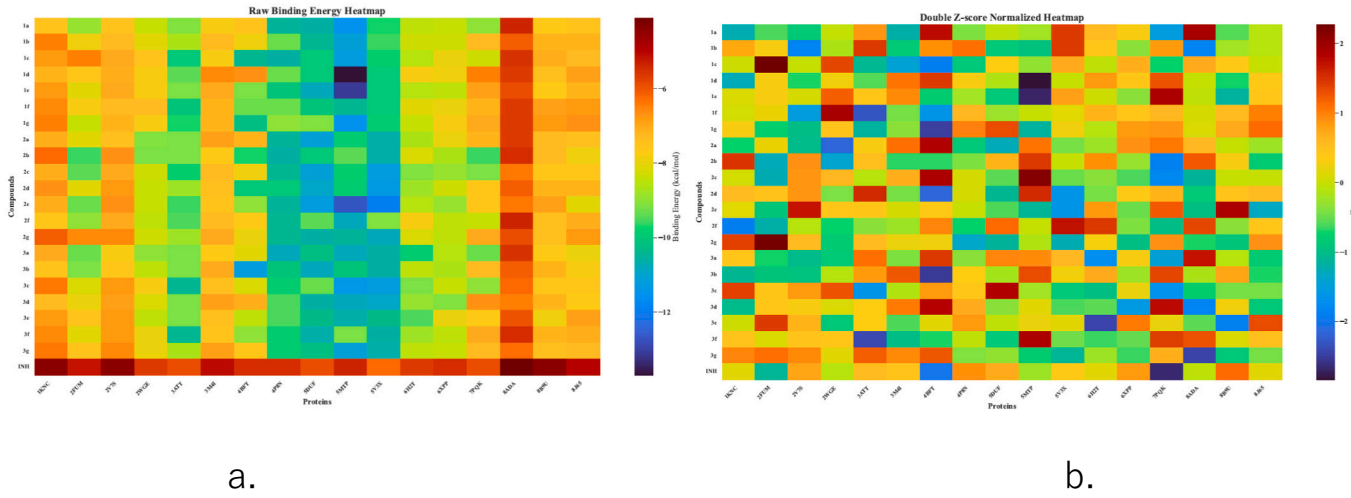

Fig. 7. Docking scores (**a**) Raw binding energies, (**b**) Standardized values. On the heat maps, rows (ligands) and columns (proteins). Isoniazid (INH) is included as a reference drug.

Table 5
: Represents the interactions of compound **1d**, **1e**, and **2e** against 8ADA and 1KNC(lowest performing proteins according to the heat map).

PROTEIN	COMPOUNDS	INTERACTIONS
8ADA	**1d**	ASP29, VAL72, SER69, LY68, ASP26
	1e	ASP54, ARG57, ILE49, VAL53, MET70, GLY50, TRP63
	2e	ARG58, VAL27, LYS21, PHE52, GLN30, SER25
1KNC	**1d**	ARG148,ILE151, LEU134, LEU155, PHE122, PHE152
	1e	PHE152, ARG148, GLU138, VAL135, LEU134, ILE151
	2e	PHE152, GLU138, LEU155, ILE151, ARG148

substituents on the phosphonium head. The triazole ring shifts to interact with GLY96 and ILE95 at the entrance of the active site, while one of the p-tolyl rings engages ILE21 and ALA22. The *meta*-chlorobenzyl group maintains interactions with ILE16 and PHE41. This demonstrates how substituents on the phosphonium core can modulate the binding pose while retaining high affinity. A critical common feature is the engagement of essential catalytic residues. All three compounds interact with TYR158, PHE149, and MET199. These are residues vital for substrate binding and cofactor (NAD+) orientation [64],[65]. They also form contacts with ILE194 and SER94, which are part of the active site. This pattern mirrors interactions observed with known slow, tight-binding InhA inhibitors, suggesting a similar, potentially potent inhibitory mechanism [66,67]. The standard drug isoniazid (INH), used as a reference, also docked within the active site but formed a less extensive interaction network, primarily reliant on hydrogen bonding, which correlates with its computationally lower binding affinity compared to **1d**, **1e**, and **2e**.

3.3.3. Molecular mechanics-generalized born surface area (MM/GBSA)

The MM/GBSA energy decomposition analysis offers explanations for the binding interactions between selected compounds and InhA (PDB

ID: 5MTP). The overall ΔG total of complexes was derived from various interactions, including Coulombic energy, covalent interactions, hydrogen bonds, lipophilic binding, π-π packing interactions, generalized Born electrostatic solvation energy, and Van der Waals energy [68] (Table 6). Compounds **1d** and **1e** demonstrated the most favorable total binding free energies, significantly more negative than those of the standard drug isoniazid (INH), suggesting stronger affinity for InhA. The main reasons for the strong binding of **1d** and **1e** are Van der Waals interactions, steric packing and their ability to mix well with fats, which are much stronger than those of INH. Compound **2e** however yields relatively weaker binding free energy as a result of its hydrophobic surface area. All three compounds ultimately achieve their enhanced binding energies predominantly through Van der Waals and lipophilic contributions. This is consistent with the behavior of phosphonium salts due to their bulky and cationic aromatic nature. This increases their π–π stacking capabilities, dispersion forces and hydrophobicity in the binding pocket. The big differences between the compounds and isoniazid show that the compounds are fitting better into the hydrophobic pockets of the enzyme, creating strong non-polar connections that hold the ligands in place at the binding site. Both **1d** and **1e** show high positive solvation energy values, suggesting some desolvation penalty upon binding, yet this is outweighed by the strong Van der Waals interactions and lipophilic energies [69]. INH shows a lower positive solvation energy, reflecting less desolvation cost but also correlating with its overall weaker binding. Compounds **1d** and **1e** recorded higher positive covalent energy values, indicating that they are in strained shapes to fit into the binding site of the InhA protein. The van der Waals and lipophilic contributions for **1d** and **1e** are consistent with these ligands stabilizing protein flexibility and thus lowering the entropic penalty associated with complex formation. This is an effect often seen with large, hydrophobic inhibitors that lock the active site into a catalytically inactive topology. This stabilization may also contribute to improved residence time, a key parameter in antimicrobial efficacy not directly captured by the docking scores. The degree of Coulombic and hydrogen bond contributions further confirms the mode of binding as hydrophobically driven which is distinct from that of isoniazid. This internal strain could be due to torsional adjustments or geometric distortions. However, INH (isoniazid) showed a very small amount of energy change when it binds, meaning it attaches without causing much change to the structure. The hydrogen bonding effects observed for compounds **1d** and **1e** were relatively weak, indicating that polar interactions are not the primary mode of binding to the active site residues. This observation is further supported by the molecular docking results (Fig. 7–9). In comparison, INH shows a stronger hydrogen bonding effect of −1.07 kcal/mol, which shows how it interacts with important catalytic residues through polar contacts (Table 6, Fig. 9). The free binding energies from the simulation confirmed how strongly the ligands bind to the target and how they interact favorably with *M. tuberculosis* InhA, as seen in the docking studies.

3.3.4. Molecular dynamic simulations

Molecular dynamics (MD) simulations were conducted over 100 ns to investigate the stability, conformational dynamics, and binding characteristics of the protein-ligand complexes formed between *Mycobacterium tuberculosis* InhA (PDB ID: 5MTP) and the most potent phosphonium salts (**1d**, **1e**, **2e**). The apo form of the enzyme was also simulated as a control. The analysis, based on root mean square deviation (RMSD), root mean square fluctuation (RMSF), radius of gyration (Rg), solvent accessible surface area (SASA), and free energy landscape (FEL) projections, provides a detailed mechanistic understanding of ligand-induced effects on InhA [70,71].

3.3.4.1. Structural stability and convergence analysis. The stability of the protein backbone in each complex was first assessed by monitoring the Cα-atom RMSD relative to the initial minimized structure (Fig. 10a). The apo-InhA system exhibited a stable trajectory with a mean RMSD of 0.253 nm and a low standard deviation of 0.024 nm, indicating a consistent native conformation throughout the simulation. Upon binding, all ligand-complexed systems showed an increase in backbone flexibility, reflected in higher mean RMSD values. The **1d**-InhA complex demonstrated the most stable binding profile among the ligands, with a mean protein-ligand RMSD of 0.347 nm and a standard deviation of 0.037 nm. Although this represents a 37 % increase in RMSD compared to the apo form, the trajectory plateaued after approximately 20 ns and maintained a tight fluctuation range, signifying a stable equilibrium state was achieved. This correlates with the strong binding affinity observed for **1d** in docking and MM-GBSA studies, suggesting the ligand induces a specific, well-defined conformation in the protein that is maintained dynamically [72,73]. In contrast, the **1e**-InhA complex displayed greater conformational adjustment, with a mean RMSD of 0.438 nm and a higher standard deviation of 0.056 nm. The 73 % increase in RMSD relative to apo-InhA indicates that **1e** binding perturbs the protein structure more significantly than **1d**. The **2e**-InhA complex presented an intermediate stability profile with a mean RMSD of 0.391 nm.

Ligand positional stability within the binding pocket was evaluated by measuring the RMSD of the ligand's heavy atoms relative to its starting pose. Compound **1d** demonstrated exceptional stability, with a remarkably low mean ligand RMSD of 0.140 nm and minimal fluctuation (Std: 0.024 nm). This indicates that once docked, **1d** maintains its orientation and interactions with key active site residues like TYR158, PHE149, and MET199 with high fidelity. Compound **1e** showed moderate positional stability (mean RMSD: 0.185 nm), while **2e** exhibited higher mobility within the pocket (mean RMSD: 0.153 nm). The superior positional stability of **1d** directly supports the molecular docking observations and provides a dynamic rationale for its potent inhibitory activity; a stable ligand pose ensures sustained occupation of the catalytic site, effectively blocking substrate access.

3.3.4.2. Residue-specific flexibility and binding site dynamics. To understand local flexibility changes induced by ligand binding, the RMSF of protein Cα atoms was calculated (Fig. 10b). The overall flexibility of the protein backbone increased for all ligand-bound states compared to the apo form. The apo-InhA exhibited a mean overall RMSF of 0.102 nm. The **1d**-bound state showed a slight decrease in global flexibility (mean RMSF: 0.091 nm, −10.8 % change), suggesting a slight tightening or stabilization of the overall structure upon **1d** binding. Conversely, **1e** and **2e** complexes showed increased global flexibility (+1.8 % and + 36.6 %, respectively).

Critical insight was gained by analyzing fluctuations in key binding site residues (TYR158, PHE149, MET199, ILE194, SER94) and others lining the active site. In the **1d**-InhA complex, the RMSF values for these key residues were consistently lower than in the apo state, with a mean key residue RMSF of 0.076 nm *versus* 0.097 nm for apo (a − 21.7 % reduction). Specifically, PHE149 (0.066 nm), TYR158 (0.106 nm), and

Table 6
The contribution of different energy components to the total MMGBSA binding free energy between the InhA subunit and the compounds.

Compound	Bind	Coulomb	Covalent	H-bond	Lipo	Packing	Solv_GB	vdW
1d	−64.98	−0.23	17.79	−0.02	−48.77	−1.41	21.76	−54.10
1e	−61.12	10.00	17.37	−0.03	−48.90	−2.86	17.55	−54.25
2e	−35.32	5.72	13.00	−0.05	−40.43	−1.80	20.68	−32.44
INH	−31.03	−9.81	0.71	−1.07	−7.31	−0.54	7.17	−20.18

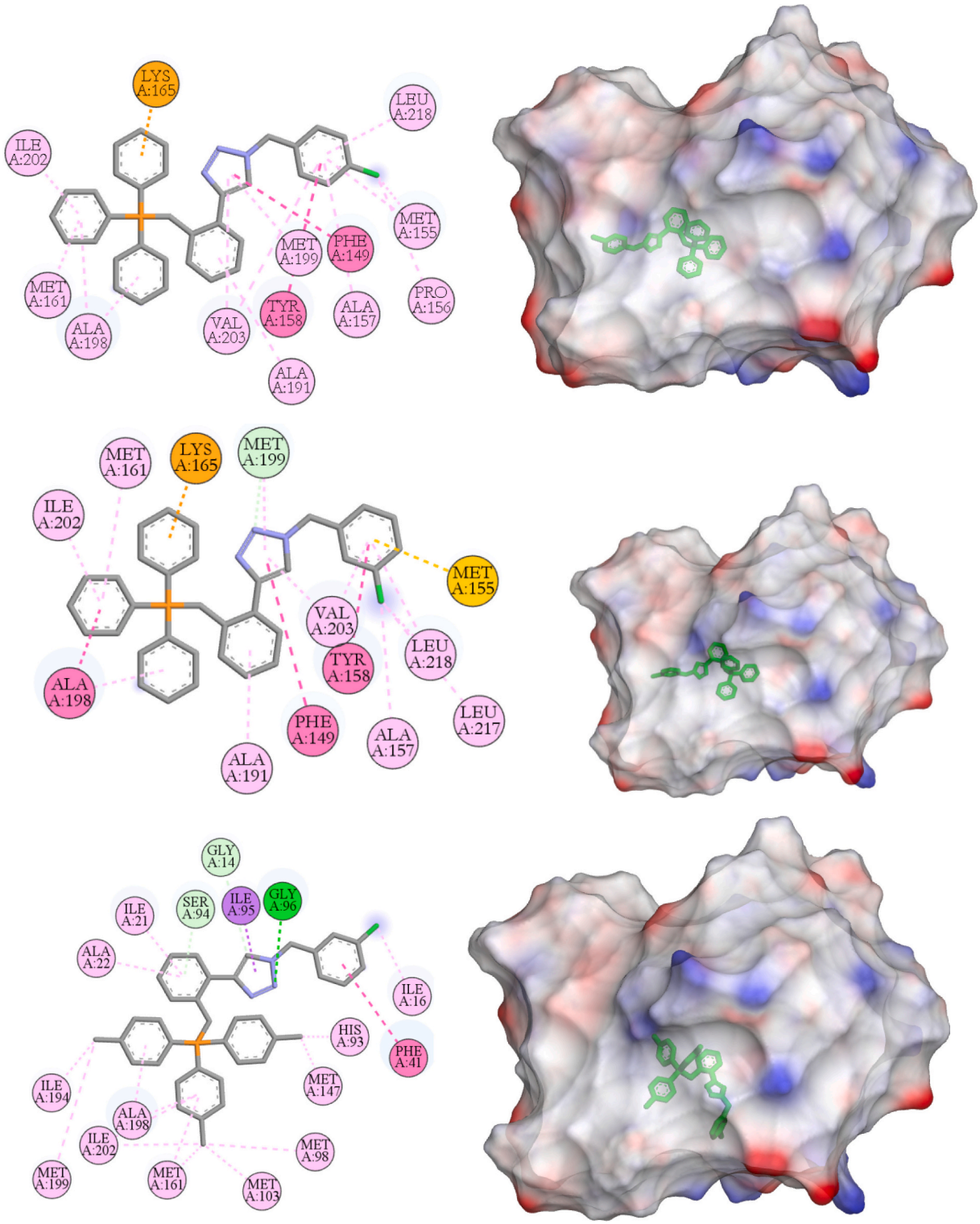

Fig. 8. a. Left: 2D interaction diagram illustrating key hydrogen bonds (green dashed lines) and hydrophobic contacts (pink dashed lines) between **1d** and the surrounding residues within the 5MTP active site. Right: Molecular electrostatic potential map between compound **1d** and protein target InhA (5MTP). b. Left: 2D interaction diagram illustrating key hydrogen bonds (green dashed lines) and hydrophobic contacts (pink dashed lines) between **1e** and the surrounding residues within the 5MTP active site. Right: Molecular electrostatic potential map between compound **1e** and protein target InhA (5MTP). c. Left: 2D interaction diagram illustrating key hydrogen bonds (green dashed lines) and hydrophobic contacts (pink dashed lines) between **2e** and the surrounding residues within the 5MTP active site. Right: Molecular electrostatic potential map between compound **2e** and protein target InhA (5MTP). (For interpretation of the references to colour in this figure legend, the reader is referred to the web version of this article.)

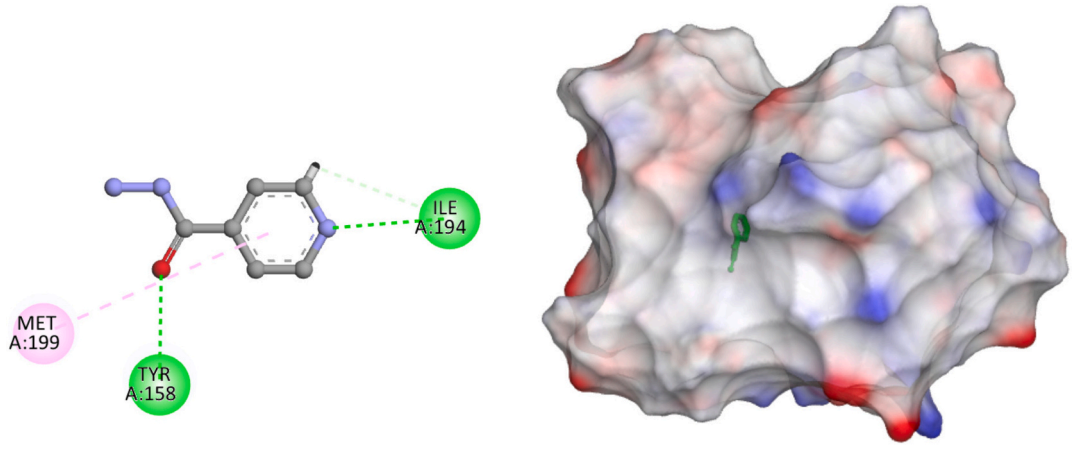

Fig. 9. Left: 2D interaction diagram illustrating key hydrogen bonds (green dashed lines) and hydrophobic contacts (pink dashed lines) between ISONIAZID and the surrounding residues within the 5MTP active site. Right: Molecular electrostatic potential map between isoniazid (INH) and protein target InhA (5MTP). (For interpretation of the references to colour in this figure legend, the reader is referred to the web version of this article.)

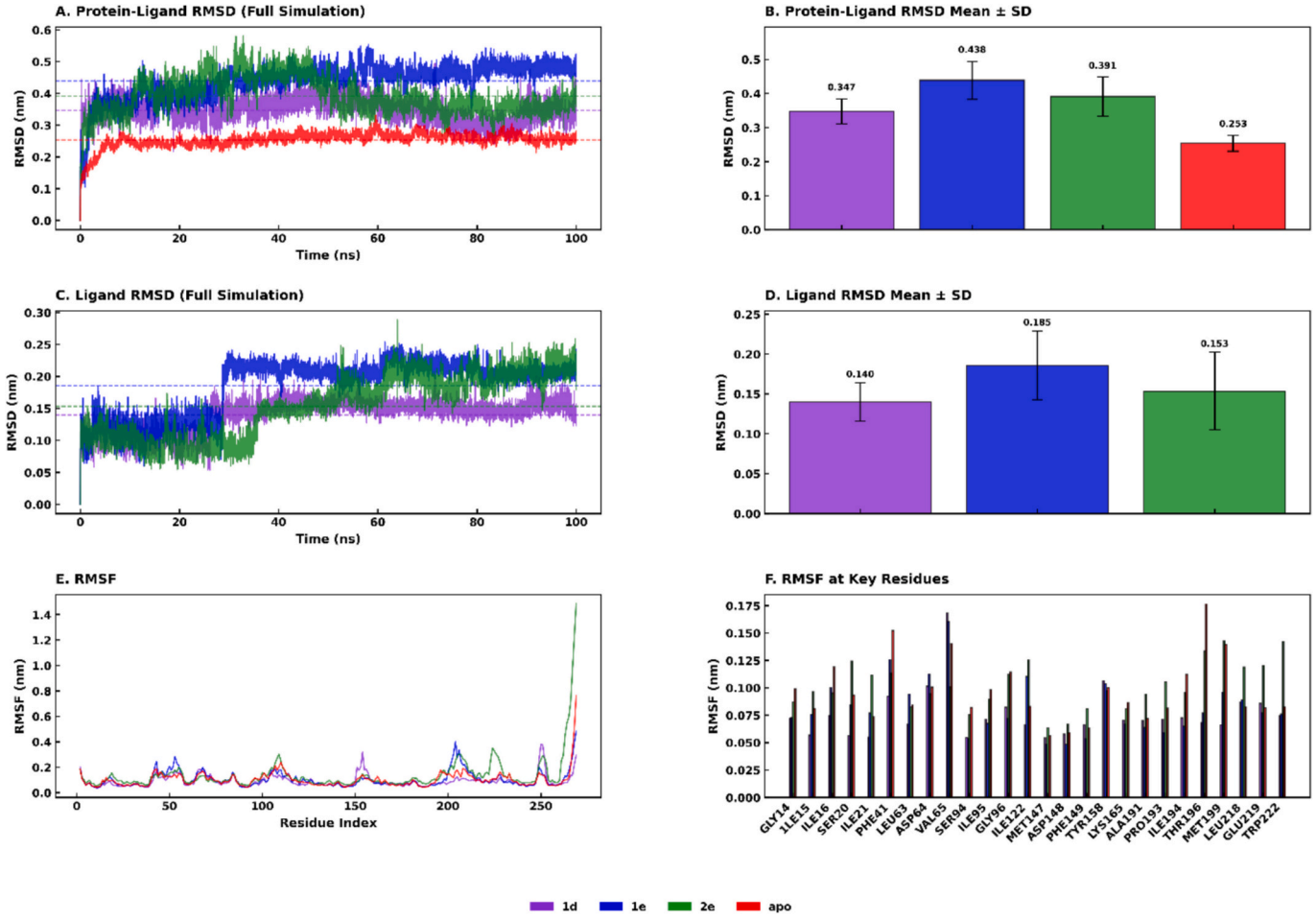

Fig. 10. Structural stability and flexibility analysis of protein–ligand complexes over a 100 ns molecular dynamics simulation. Panels show (A) full protein–ligand RMSD trajectories, (B) protein–ligand RMSD mean ± SD, (C) ligand-only RMSD trajectories, (D) ligand RMSD mean ± SD, (E) residue-level RMSF, and (F) RMSF at key active-site residues for the apo protein and complexes

MET199 (0.066 nm) all exhibited reduced mobility. This damping of flexibility indicates that **1d** engages these residues in strong, stabilizing interactions such as hydrophobic and van der Waals contacts as seen in docking which effectively lock them into a conformation favorable for inhibition. For the **1e** complex, key residue flexibility was also reduced relative to apo (mean: 0.082 nm, −15.3 % change), though not as markedly as with **1d**. Residues like ILE16 and ILE122 showed increased flexibility, suggesting **1e** could cause localized adjustments upon binding. The **2e** complex presented a unique profile. While the mean key residue flexibility was slightly higher than apo (0.102 nm, +5.4 %

change), specific residues like ILE194 and MET199 became significantly more flexible (+31.1 % and + 72.9 %, respectively). This induced flexibility, particularly around MET199 and the adjacent loop, may be linked to the presence of the p-tolyl methyl groups on the phosphonium head of **2e**, which could create subtle steric pressures or alter packing within the hydrophobic pocket. A pronounced effect was observed in the loop region encompassing residues 65–75, which includes the catalytic loop. In the apo and INH-bound states, this region displayed moderate flexibility. However, in all phosphonium salt complexes, particularly with **1d** and **1e**, this loop exhibited reduced fluctuation. This stabilization of a functionally important mobile loop further underscores the profound impact of these bulky ligands on the enzyme's dynamic architecture, potentially restricting conformational changes necessary for catalysis.

3.3.4.3. Structural compactness and solvent exposure. The radius of gyration (Rg) and solvent accessible surface area (SASA) provide metrics for global structural compactness and hydration (Fig. 10c, d) [74]. The apo-InhA had a mean Rg of 1.833 nm and a mean SASA of 134.54 nm^2. Binding of **1d** resulted in a negligible change in compactness (Rg: 1.839 nm) but a notable 2.3 % reduction in SASA (131.47 nm^2). This decrease in solvent-accessible surface indicates that **1d** binding causes a tightening of the protein structure or more effectively buries hydrophobic regions, consistent with its extensive network of non-polar interactions within the deep binding pocket. Compound **1e** had virtually identical Rg and SASA values to the apo enzyme, indicating it does not significantly alter the global fold or surface exposure. Compound **2e**, however, induced a measurable expansion of the protein structure, with the highest mean Rg of 1.858 nm (+1.3 % *vs* apo), while its SASA remained similar to apo. This suggests **2e** binding may cause a slight opening or loosening of the tertiary structure, corroborating the increased flexibility observed in its RMSF profile. The fluctuation in these parameters, measured by their standard deviations, also informs on structural rigidity. The **1d** complex showed the lowest fluctuation in both Rg (Std: 0.0066 nm) and SASA (Std: 2.38 nm^2), indicating a highly stable, rigid conformation throughout the simulation. The **2e** complex displayed the highest Rg fluctuation (Std: 0.0170 nm), aligning with its less stable binding signature. The "packing efficiency," inferred from low SASA fluctuation and stable Rg, is highest for the **1d** complex, suggesting optimal complementary surface burial between the ligand and the InhA binding site.

Principal Component Analysis (PCA) was performed on the Cα-atom trajectories to elucidate the dominant collective motions of InhA and to quantify the impact of ligand binding on the protein's essential dynamics. The first two principal components (PC1 and PC2), which together capture the most significant conformational fluctuations, were analyzed for the apo enzyme and its complexes with compounds **1d**, **1e**, and **2e**. The analysis was conducted on the first 100 ns of each simulation, comprising 10,001 frames per system sampled at 0.01 ns intervals. The conformational space explored by each system, defined by the projection of the trajectory onto the PC1 and PC2 plane, reveals distinct patterns of motion (Table 7: PCA Conformational Sampling Metrics). The apo-InhA system sampled a broad conformational landscape, with a convex hull area of 21.48 arbitrary $units^2$ and a perimeter of 17.13. The radius of gyration of this distribution, a measure of its spread in the PC space, was 1.65. The ranges of motion along PC1 (6.16) and PC2 (4.53) were substantial, confirming the inherent flexibility of the unliganded enzyme. Approximately 68 % of the simulation frames fell within one standard deviation of the mean along each PC, indicating a coherent but wide sampling of its native conformational ensemble. Binding of the phosphonium salts systematically restricted this native flexibility. The **1d**-InhA complex exhibited the most confined motion. The convex hull area occupied by this complex (16.56 $units^2$) was 23 % smaller than that of the apo form. Similarly, the perimeter (15.60) and the radius of gyration of the distribution (1.64) decreased. The ranges along PC1 (5.28) and PC2 (4.40) were notably reduced. Critically, 83.3 % of frames were within one standard deviation along PC2, and 99.97 % were within two standard deviations along PC1, demonstrating an exceptionally tight clustering of conformations. This indicates that **1d** binding effectively suppresses a major mode of the protein's intrinsic motion, locking it into a narrow, well-defined conformational subspace. The **1e**-InhA complex presented a more moderate constriction of dynamics. While its PC1 range (6.20) was comparable to the apo state, its PC2 range expanded significantly to 8.50, the largest among all systems. This resulted in the largest convex hull area (38.97 $units^2$), an 81 % increase over apo. However, the radius of gyration for this distribution was also the highest at 2.23, signifying that the sampled conformations, while numerous, are dispersed. This suggests that **1e** binding does not restrict global motion to the same degree as **1d**, instead, it permits or even facilitates movement along specific collective coordinates (PC2) while potentially restricting others. This altered dynamic profile represents a distinct ligand-induced state. Compound **2e** explored an extremely wide range along PC1 (12.96), more than double that of the apo enzyme, while the PC2 range remained high (8.50). This produced the largest conformational landscape by area (74.45 $units^2$) and perimeter (34.42). The radius of gyration for this distribution was 4.73, indicating a vast spread of sampled conformations in the essential subspace. Interestingly, despite this broad exploration, the sampling was efficient, with 100 % of frames within two standard deviations along PC1. This pattern signifies that **2e** binding redirects the protein's dominant motions, amplifying fluctuations along PC1, a mode that is likely functionally relevant for substrate binding or product release, while maintaining a coherent trajectory within this new, expansive dynamic regime. The lack of correlation between PC1 and PC2 (covariance ≈ 0) in all ligand-bound systems confirms that these two dominant motions are independent [75].

3.3.4.4. Conformational free energy landscape and binding mechanism. To elucidate the conformational ensembles sampled during binding, the free energy landscape (FEL) was projected onto the first two principal components (PC1 and PC2) of protein backbone motion (Table: Free Energy Landscape Analysis) (Fig. 11). The apo-InhA sampled a broad, rugged energy landscape with 84 local minima and a high-energy barrier of 15.4 kT, reflecting the inherent flexibility and multiple sub-states of the unliganded enzyme. The binding of **1d** dramatically reshaped this landscape. The **1d**-InhA complex populated a more confined, lower-energy basin centered at PC1 = -1.17, PC2 = 0.25. While the landscape remained rugged (75 minima), the global minimum was deeper relative to the sampled ensemble, and the system spent a higher fraction of time (7.13 %) in stable, low-energy basins (defined within 3 kT of the global minimum). This indicates that **1d** binding selectively stabilizes a specific conformational sub-state of InhA, reducing its entropy and effectively trapping the enzyme in a non-productive conformation. The significant reduction in the conformational heterogeneity index (from

Table 7
: Comparative structural stability metrics for the apo system and ligand-bound complexes, including radius of gyration, solvent-accessible surface area (SASA).

System	Rg (nm) (mean ± SD)	SASA (nm^2) (mean ± SD)	Compactness ratio	Rg fluctuation (%)	SASA fluctuation (%)
Apo	1.8334 ± 0.0107	134.5431 ± 3.0690	0.0458	4.03	16.11
1d	1.8386 ± 0.0066	131.4682 ± 2.3846	0.0473	2.67	13.24
1e	1.8337 ± 0.0089	134.9565 ± 2.5564	0.0457	3.45	13.20
2e	1.8576 ± 0.0170	134.8436 ± 3.0740	0.0475	4.60	14.35

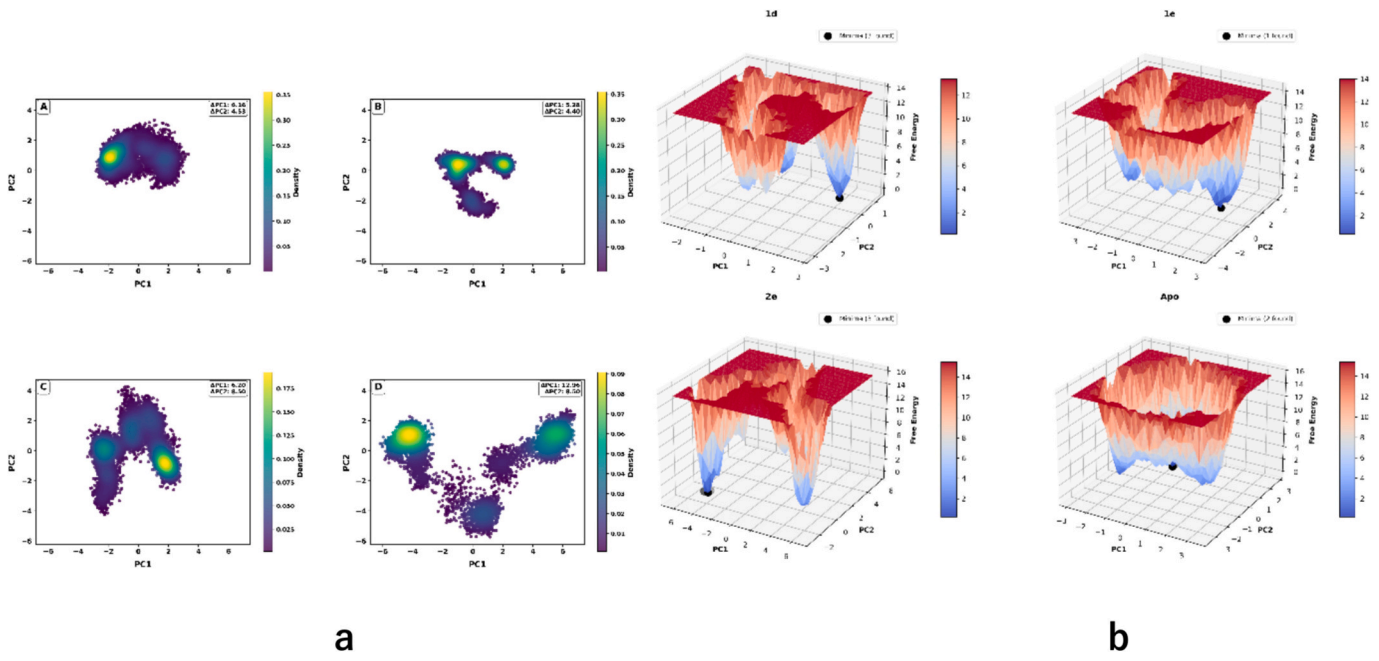

Fig. 11. (a) Two-dimensional PCA density projections for the apo protein and ligand-bound complexes. Panels A–D illustrate the distribution of conformational states sampled along PC1 and PC2, revealing distinct cluster patterns and ligand-specific structural shifts. (b) Three-dimensional free-energy landscapes (FELs) mapped along PC1 and PC2 for the same systems. Panels A–D show the conformational basins and energy minima, highlighting differences in structural stability and the depth of energy wells between the apo and ligand-bound states.

416.6 for apo to 296.9 for **1d**) quantifies this ligand-induced focusing of the conformational ensemble. The FEL for the **1e** complex also showed stabilization, with 77 minima and a stable basin fraction of 4.10 %. Its global minimum was displaced on the PC axis from that of **1d**, indicating it stabilizes a distinct, though also inhibitory, protein conformation. The **2e** complex presented the most restricted conformational landscape among the ligands, with the fewest local minima (69) and the lowest heterogeneity index (262.8). However, its stable basin fraction was lower (2.73 %), and its mean energy across the landscape was the highest (13.04 kT). This suggests that while **2e** restricts the protein's motion, the resulting dominant conformation may be somewhat strained or higher in energy, which could correlate with its slightly lower binding affinity compared to **1d** and **1e**.

The phosphonium salts function as molecular wedges that stabilize the InhA active site, effectively clamping down on flexible elements like the substrate-binding loop and catalytic residues. This mechanism, which involves dynamic stabilization and entropy reduction, explains their strong efficacy against drug-sensitive and multidrug-resistant strains, making them potential scaffolds for new, long-residence-time InhA inhibitors [41].

4. Conclusions

A series of twenty-one phosphonium salt hybrids were successfully synthesized *via* a Cu(I)-catalyzed azide–alkyne cycloaddition (CuAAC) click reaction. Biological evaluation identified compounds **1d**, **1e**, and **2e** as potent inhibitors of *Mycobacterium tuberculosis* H37Rv, with **1d** and **1e** achieving 100 % inhibition at 6.25 μg/mL. Compound **2e** exhibited the highest selectivity towards mycobacteria over murine macrophages, while **3f** showed notable cytotoxicity. Computational studies revealed that the most active compounds preferentially target enoyl-acyl carrier protein reductase (InhA), a key enzyme in mycolic acid biosynthesis. Molecular docking and MM/GBSA calculations confirmed strong binding to critical active-site residues (TYR158, PHE149, MET199, ILE194, SER94). Molecular dynamics simulations further demonstrated that **1d** acts as a dynamic stabilizer, drastically restricting InhA's conformational flexibility and trapping it in a catalytically inactive state. Although the compounds generally exhibit favorable predicted drug-likeness and oral bioavailability, some toxicity concerns highlight the need for further structural optimization. These findings collectively establish click-tethered phosphonium salts particularly **1d** as promising lead candidates for the development of novel anti-tubercular agents targeting InhA through a mechanism of dynamic stabilization.

CRediT authorship contribution statement

Cedric Dzidzor Kodjo Amengor: Methodology, Formal analysis, Data curation, Conceptualization. **Prince Danan Biniyam:** Writing – review & editing, Formal analysis, Data curation. **Victoria Ohene-Adu:** Methodology, Formal analysis. **Kwabena Adu-Adjei:** Methodology, Formal analysis. **Michael Osei:** Methodology, Formal analysis. **Patrick Gyan:** Methodology, Investigation, Formal analysis. **Paul Quansah:** Methodology, Investigation, Formal analysis, Data curation. **Felix Odame:** Formal analysis, Data curation. **Ernest Oyeh:** Writing – review & editing, Visualization. **Cyril Makafui Amengor:** Writing – review & editing, Software, Resources. **Lawrence Sheringham Borquaye:** Validation, Data curation.

Declaration of competing interest

The authors declare that they have no known competing financial interests or personal relationships that could have appeared to influence the work reported in this paper.

Acknowledgements

The authors express their gratitude to the technicians of the Synthetic Medicinal Chemistry and Computational Division at the School of Pharmacy, University of Health and Allied Sciences.

The authors also want to thank the technical staff at the Cell Culture and Microbiology Unit at the Department of Pharmacology, KNUST, for their expertise.

Appendix A. Supplementary data

Supplementary data to this article can be found online at https://doi.org/10.1016/j.bioorg.2025.109390.

Data availability

The data that supports the findings of this study are available in the supplementary material of this article.

References

[1] D.E. Bloom, D. Cadarette, Infectious disease threats in the twenty-first century: strengthening the global response, Front. Immunol. 10 (2019) 549.
[2] B. Baral, K. Mamale, S. Gairola, C. Chauhan, A. Dey, R.K. Kaundal, Infectious diseases and its global epidemiology, in: Nanostructured Drug Delivery Systems in Infectious Disease Treatment, Academic Press, 2024, pp. 1–24.
[3] D.L. Heymann, G.R. Rodier, Hot spots in a wired world: WHO surveillance of emerging and re-emerging infectious diseases, Lancet Infect. Dis. 1 (5) (2001) 345–353.
[4] R.A. Cash, V. Narasimhan, Impediments to global surveillance of infectious diseases: consequences of open reporting in a global economy, Bull. World Health Organ. 78 (2000) 1358–1367.
[5] A. Kanchar, S. Swaminathan, Tuberculosis control: WHO perspective and guidelines, The Indian Journal of Pediatrics 86 (2019) 703–706.
[6] K. Yadav, S. Prakash, Tuberculosis: an airborne disease, Global journal of Microbiology research 5 (5) (2017) 225–243.
[7] S.H. Lee, Tuberculosis infection and latent tuberculosis, Tuberculosis and respiratory diseases 79 (4) (2016) 201.
[8] A.M. Metry, I. Al Salmi, S. Al-Abri, F. Al Ismaili, Y. Al Mahrouqi, A. Hola, F. A. Shaheen, Epidemiology and outcome of tuberculosis in immunocompromised patients, Saudi J. Kidney Dis. Transpl. 28 (4) (2017) 806–817.
[9] K. Floyd, P. Glaziou, A. Zumla, M. Raviglione, The global tuberculosis epidemic and progress in care, prevention, and research: an overview in year 3 of the end TB era, Lancet Respir. Med. 6 (4) (2018) 299–314.
[10] J. Bruchfeld, M. Correia-Neves, G. Källenius, Tuberculosis and HIV coinfection, Cold Spring Harb. Perspect. Med. 5 (7) (2015) a017871.
[11] M. Gjergji, J. Bushati, A. Harxhi, H. Hafizi, P. Pipero, Tuberculosis in HIV/AIDS patients, Adv Tech Clin Microbiol 1 (3) (2017) 16.
[12] P.S. Nyasulu, C.O. Doumbia, V. Ngah, A.C.G. Togo, B. Diarra, G. Chongwe, Multidrug-resistant tuberculosis: latest opinions on epidemiology, rapid diagnosis, and management, Curr. Opin. Pulm. Med. 30 (3) (2024) 217–228.
[13] M.B.T. Brigaste, L.A. Teh, The battle continues: an interpretative phenomenological analysis of the experiences of multidrug-resistant tuberculosis (MDR-TB) patients, Psychol. Stud. 63 (2018) 9–18.
[14] J.D.C.O. Sardi, C.R. Polaquini, I.A. Freires, L.C.D.C. Galvão, J.G. Lazarini, G. S. Torrezan, P.L. Rosalen, Antibacterial activity of diacetylcurcumin against Staphylococcus aureus results in decreased biofilm and cellular adhesion, J. Med. Microbiol. 66 (6) (2017) 816–824.
[15] Y. Zhang, C. Vilchèze, J.R. Jacobs, W. R., Mechanisms of drug resistance in Mycobacterium tuberculosis, Tuberculosis and the tubercle bacillus (2004) 115–140.
[16] J.A. Caminero, A. Scardigli, Classification of antituberculosis drugs: a new proposal based on the most recent evidence, Eur. Respir. J. 46 (4) (2015) 887–893.
[17] J.C. Palomino, A. Martin, Drug resistance mechanisms in Mycobacterium tuberculosis, Antibiotics 3 (3) (2014) 317–340.
[18] A. Sahu, P. Sahu, R. Agrawal, A recent review on drug modification using 1, 2, 3-triazole, Curr. Chem. Biol. 14 (2) (2020) 71–87.
[19] - H. Zhou, C.Y. Wang, Recent researches in triazole compounds as medicinal drugs, Curr. Med. Chem. 19 (2) (2012) 239–280.
[20] G. Pavale, P. Acharya, N. Korgavkar, M.M.V. Ramana, Design, synthesis, and biological evaluation of quinoxaline-bearing tetrahydropyridine derivatives as anticancer, antioxidant, and anti-tubercular agents, Curr. Comput. Aided Drug Des. 18 (6) (2022) 414–424.
[21] A. Sharma, A.K. Agrahari, S. Rajkhowa, V.K. Tiwari, Emerging impact of triazoles as anti-tubercular agents, Eur. J. Med. Chem. 238 (2022) 114454.
[22] P.S. Phatak, R.D. Bakale, R.S. Kulkarni, S.T. Dhumal, P.P. Dixit, V.S. Krishna, K. P. Haval, Design and synthesis of new indanol-1, 2, 3-triazole derivatives as potent antitubercular and antimicrobial agents, Bioorg. Med. Chem. Lett. 30 (22) (2020) 127579.
[23] P.S. Patil, S.L. Kasare, N.B. Haval, V.M. Khedkar, P.P. Dixit, E.M. Rekha, K. P. Haval, Novel isoniazid embedded triazole derivatives: synthesis, antitubercular and antimicrobial activity evaluation, Bioorg. Med. Chem. Lett. 30 (19) (2020) 127434.
[24] X. Meng, K.J. Edgar, "Click" reactions in polysaccharide modification, Prog. Polym. Sci. 53 (2016) 52–85.
[25] A.P. Silvestri, Development and Application of Metal-Mediated Bioorthogonal Ligations, The Scripps Research Institute, 2018.
[26] F.K. Kekessie, C.D.K. Amengor, A. Brobbey, J.N. Addotey, C.A. Danquah, P. Peprah, M. Tetteh, Synthesis, molecular docking studies and ADME prediction of some new triazoles as potential antimalarial agents, Scientific African 14 (2021) e00998.
[27] V.V. Ermolaev, D.M. Arkhipova, V.A. Miluykov, A.P. Lyubina, S.K. Amerhanova, N. V. Kulik, V.P. Ananikov, Sterically hindered quaternary phosphonium salts (QPSs): antimicrobial activity and hemolytic and cytotoxic properties, Int. J. Mol. Sci. 23 (1) (2021) 86.
[28] C.D. Kodjo Amengor, C. Amaning Danquah, E.B.A. Adusei, F.K. Kekessie, F. Ofosu-Koranteng, P. Peprah, Y. Saaka, Synthesized phosphonium compounds demonstrate resistant modulatory and antibiofilm formation activities against some pathogenic bacteria, Heteroat. Chem. 2022 (1) (2022) 7411957.
[29] J. Khan, A. Rani, M. Aslam, R.S. Maharia, G. Pandey, B. Nand, Exploring triazole-based drugs: synthesis, application, FDA approvals, and clinical trial updates-a comprehensive review, Tetrahedron 134122 (2024).
[30] C.E. Diesendruck, L. Zhu, J.S. Moore, Alkyne mechanochemistry: putative activation by transoidal bending, Chem. Commun. 50 (87) (2014) 13235–13238.
[31] S. Borrell, A. Trauner, D. Brites, L. Rigouts, C. Loiseau, M. Coscolla, S. Gagneux, Reference set of Mycobacterium tuberculosis clinical strains: a tool for research and product development, PloS One 14 (3) (2019) e0214088.
[32] P.J. Brennan, Structure, function, and biogenesis of the cell wall of Mycobacterium tuberculosis, Tuberculosis 83 (1–3) (2003) 91–97.
[33] R. Miggiano, C. Morrone, F. Rossi, M. Rizzi, Targeting genome integrity in Mycobacterium tuberculosis: from nucleotide synthesis to DNA replication and repair, Molecules 25 (5) (2020) 1205.
[34] S.S. Butt, Y. Badshah, M. Shabbir, M. Rafiq, Molecular docking using chimera and autodock vina software for nonbioinformaticians, JMIR Bioinformatics and Biotechnology 1 (1) (2020) e14232.
[35] R. Kannadasan, M.S. Saleembasha, I.A. Emerson, A frame work for learning drug designing through molecular modelling software techniques and biological databases for protein-ligand interactions, Int. J. Eng. Res. Afr. 27 (2016) 111–118.
[36] Ferrari, I. V., & Patrizio, P. (2021). Docking molecular analysis of potential aldosterone antagonists. bioRxiv, 2021-07.
[37] J.J. Sahayarayan, K.S. Rajan, R. Vidhyavathi, M. Nachiappan, D. Prabhu, S. Alfarraj, A.N. Daniel, In-silico protein-ligand docking studies against the estrogen protein of breast cancer using pharmacophore based virtual screening approaches, Saudi Journal of Biological Sciences 28 (1) (2021) 400–407.
[38] O. Trott, A.J. Olson, AutoDock Vina: improving the speed and accuracy of docking with a new scoring function, efficient optimization, and multithreading, J. Comput. Chem. 31 (2) (2010) 455–461.
[39] E.B. Elkaeed, I.H. Eissa, H. Elkady, A. Abdelalim, A.M. Alqaisi, A.A. Alsfouk, A. M. Metwaly, A multistage in silico study of natural potential inhibitors targeting SARS-CoV-2 main protease, Int. J. Mol. Sci. 23 (15) (2022) 8407.
[40] E. Mateev, I. Valkova, B. Angelov, M. Georgieva, A. Zlatkov, Validation through re-docking, cross-docking and ligand enrichment in various well-resoluted MAO-B receptors, Int. J. Pharm. Sci. Res. 13 (2022) 1099–1107.
[41] E. Wang, H. Sun, J. Wang, Z. Wang, H. Liu, J.Z. Zhang, T. Hou, End-point binding free energy calculation with MM/PBSA and MM/GBSA: strategies and applications in drug design, Chem. Rev. 119 (16) (2019) 9478–9508.
[42] C.Y. Jia, J.Y. Li, G.F. Hao, G.F. Yang, A drug-likeness toolbox facilitates ADMET study in drug discovery, Drug Discov. Today 25 (1) (2020) 248–258.
[43] Kar, S., Roy, K., & Leszczynski, J. (2022). In silico tools and software to predict ADMET of new drug candidates. In In Silico Methods for Predicting Drug Toxicity (pp. 85–115). New York, NY: Springer US.
[44] S. Patterson, A.H. Fairlamb, Current and future prospects of nitro-compounds as drugs for trypanosomiasis and leishmaniasis, Curr. Med. Chem. 26 (23) (2019) 4454–4475.
[45] S. Saxena, H.P. Spaink, G. Forn-Cuní, Drug resistance in nontuberculous mycobacteria: mechanisms and models, Biology 10 (2) (2021) 96.
[46] R.D. Bakale, S.M. Sulakhe, S.L. Kasare, B.P. Sathe, S.S. Rathod, P.B. Choudhari, K. P. Haval, Design, synthesis and antitubercular assessment of 1, 2, 3-triazole incorporated thiazolylcarboxylate derivatives, Bioorg. Med. Chem. Lett. 97 (2024) 129551.
[47] U.V. Mhetre, N.B. Haval, G.M. Bondle, S.S. Rathod, P.B. Choudhari, J. Kumari, K. P. Haval, Design, synthesis and molecular docking study of novel triazole–quinazolinone hybrids as antimalarial and antitubercular agents, Bioorg. Med. Chem. Lett. 108 (2024) 129800.
[48] R.D. Bakale, P.S. Phatak, S.S. Rathod, P.B. Choudhari, E.M. Rekha, D. Sriram, K. P. Haval, *In vitro* and *in silico* exploration of newly synthesized triazolyl-isonicotinohydrazides as potent antitubercular agents, J. Biomol. Struct. Dyn. 43 (3) (2025) 1372–1391, https://doi.org/10.1080/07391102.2023.2291826.
[49] C. Kannigadu, D.D. N'Da, Recent advances in the synthesis and development of nitroaromatics as anti-infective drugs, Curr. Pharm. Des. 26 (36) (2020) 4658–4674.
[50] A.S. Al Wasidi, A.S. Hassan, A.M. Naglah, In vitro cytotoxicity and druglikeness of pyrazolines and pyridines bearing benzofuran moiety, Journal of Applied Pharmaceutical Science 10 (4) (2020) 142–148.
[51] D. Dahlgren, H. Lennernäs, Intestinal permeability and drug absorption: predictive experimental, computational, and in vivo approaches, Pharmaceutics 11 (8) (2019) 411.
[52] N.A. Meanwell, Improving drug candidates by design: a focus on physicochemical properties as a means of improving compound disposition and safety, Chem. Res. Toxicol. 24 (9) (2011) 1420–1456.
[53] D. Klimoszek, M. Jeleń, B. Morak-Młodawska, M. Dołowy, Evaluation of the lipophilicity of angularly condensed Diquino- and Quinonaphthothiazines as potential candidates for new drugs, Molecules 29 (7) (2024) 1683.
[54] S. Banerjee, P. Ghosh, R. Rathi, A. Ghosh, R.S. Roy, A.K. Das, Theoretical investigation of physicochemical properties, bioactivity, and toxicity of common anxiety medications, ChemistrySelect 9 (45) (2024) e202404146.

[55] S. Ma, M. McGann, I.J. Enyedy, The influence of calculated physicochemical properties of compounds on their ADMET profiles, Bioorg. Med. Chem. Lett. 36 (2021) 127825.
[56] R. Mannhold, H. Kubinyi, G. Folkers, Pharmacokinetics and Metabolism in Drug Design, John Wiley & Sons, 2012.
[57] P. Mossel, A.L. Bartels, P.P. de Deyn, G. Luurtsema, The Role of P-Glycoprotein at the Blood–Brain Barrier in Neurological and Psychiatric Disease, PET and SPECT in Psychiatry (2021) 45–81.
[58] Z. Zhang, W. Tang, Drug metabolism in drug discovery and development, Acta Pharm. Sin. B 8 (5) (2018) 721–732.
[59] A.K. Hauck, D.A. Bernlohr, Oxidative stress and lipotoxicity, J. Lipid Res. 57 (11) (2016) 1976–1986.
[60] J. Fedorowicz, J. Sączewski, Advances in the synthesis of biologically active quaternary ammonium compounds, Int. J. Mol. Sci. 25 (9) (2024) 4649.
[61] D. Yusuf, A.M. Davis, G.J. Kleywegt, S. Schmitt, An alternative method for the evaluation of docking performance: RSR vs RMSD, J. Chem. Inf. Model. 48 (7) (2008) 1411–1422.
[62] J. Sun, D.A. Decato, V.S. Bryantsev, E.A. John, O.B. Berryman, The interplay between hydrogen and halogen bonding: substituent effects and their role in the hydrogen bond enhanced halogen bond, Chem. Sci. 14 (33) (2023) 8924–8935.
[63] S.K. Wahan, G. Bhargava, V. Chawla, P.A. Chawla, Unlocking InhA: novel approaches to inhibit Mycobacterium tuberculosis, Bioorg. Chem. 146 (2024) 107250, https://doi.org/10.1016/j.bioorg.2024.107250.
[64] A. Chollet, L. Maveyraud, C. Lherbet, V. Bernardes-Génisson, An overview on crystal structures of InhA protein: apo-form, in complex with its natural ligands and inhibitors, Eur. J. Med. Chem. 146 (2018) 318–343.
[65] T. Al-Warhi, A. Sabt, M. Korycka-Machala, A.F. Kassem, M.A. Shaldam, H.A. A. Ibrahim, J. Dziadek, Benzenesulfonohydrazide-tethered non-fused and fused heterocycles as potential anti-mycobacterial agents targeting enoyl acyl carrier protein reductase (InhA) with antibiofilm activity, RSC Adv. 14 (41) (2024) 30165–30179.
[66] L.A. Spagnuolo, S. Eltschkner, W. Yu, F. Daryaee, S. Davoodi, S.E. Knudson, P. J. Tonge, Evaluating the contribution of transition-state destabilization to changes in the residence time of triazole-based InhA inhibitors, J. Am. Chem. Soc. 139 (9) (2017) 3417–3429.
[67] K. Sakthikumar, J. Dhaveethu Raja, R. Vijay Solomon, M. Sankarganesh, Density functional theory molecular modelling, DNA interactions, antioxidant, antimicrobial, anticancer, and biothermodynamic studies of bioactive water-soluble mixed ligand complexes, Journal of Biomolecular Structure and Dynamics 37 (10) (2019) 2498–2514.
[68] D.J. Huggins, W. Sherman, B. Tidor, Rational approaches to improving selectivity in drug design, J. Med. Chem. 55 (4) (2012) 1424–1444.
[69] K. Liu, E. Watanabe, H. Kokubo, Exploring the stability of ligand binding modes to proteins by molecular dynamics simulations, J. Comput. Aided Mol. Des. 31 (2017) 201–211.
[70] A. Bornot, C. Etchebest, A.G. De Brevern, Predicting protein flexibility through the prediction of local structures, Proteins: Struct., Funct., Bioinf. 79 (3) (2011) 839–852.
[71] J.J. Clark, M.L. Benson, R.D. Smith, H.A. Carlson, Inherent versus induced protein flexibility: comparisons within and between apo and holo structures, PLoS Comput. Biol. 15 (1) (2019) e1006705.
[72] A. Karshikoff, L. Nilsson, R. Ladenstein, Rigidity versus flexibility: the dilemma of understanding protein thermal stability, FEBS J. 282 (20) (2015) 3899–3917.
[73] S. Genheden, U. Ryde, The MM/PBSA and MM/GBSA methods to estimate ligand-binding affinities, Expert Opin. Drug Discovery 10 (5) (2015) 449–461.
[74] M.Y. Lobanov, N.S. Bogatyreva, O.V. Galzitskaya, Radius of gyration as an indicator of protein structure compactness, Mol. Biol. 42 (2008) 623–628.
[75] S. Ausaf Ali, M. Imtaiyaz Hassan, A. Islam, F. Ahmad, A review of methods available to estimate solvent-accessible surface areas of soluble proteins in the folded and unfolded states, Curr. Protein Pept. Sci. 15 (5) (2014) 456–476.